Solar Physics

Comprehensive Sun-to-Earth analysis of the Geoeffective Solar event of June 21, 2015: Effects on the Magnetosphere - Plasmasphere - Ionosphere system.
--Manuscript Draft--

	Matteo Martucci
	Matteo Merge'
	Ermanno Pietropaolo
	Paolo Romano
	Roberta Sparvoli
	Marco Stangalini
	Antonio Vecchio
	Massimo Vellante
	Umberto Villante
	Francesca Zuccarello
	B. Heilig
	J Reda
	J. Lichtenberger

Order of Authors Secondary Information:	
Funding Information:	

Abstract:	A full-halo coronal mass ejection left the sun on June 21, 2015 from the active region NOAA 12371 encountering Earth on June 22, 2015, generating a G3 strong geomagnetic storm. The CME was associated with an M2 class flare observed at 01:42 UT, located near the center disk (N12E16). Using satellite data from solar, heliospheric, magnetospheric missions and ground-based instruments, we performed a comprehensive Sun-to-Earth analysis. In particular, we analyzed the active region evolution using ground-based and satellite instruments (BBSO, IRIS, HINODE, SDO/AIA, RHESSI -- Halpha, EUV, UV, X), the AR magnetograms, using data from SDO HMI, the relative particle data, using PAMELA instruments and the effects of interplanetary perturbation on cosmic ray intensity. We also evaluated the 1-8 $\AA$ soft X-ray and low-frequenct ($\sim$ 1 MHz) Type III radio burst time-integrated intensity (or fluence) of the flare in order to make a prediction of the associated Solar Energetic Particle (SEP) event by using the model developed by \cite{Laurenza09}. In addition, using ground based observations from lower to higher latitudes (INTERMAGNET - EMMA, etc.), we reconstructed the ionospheric current system associated to the geomagnetic Sudden Commencement. Furthermore, SuperDARN measurements are used to image the global ionospheric polar convection during the SSC and during the principal phases of the geomagnetic storm. Moreover, we investigated the dynamics of the plasmasphere during the different phases of the geomagnetic storm by examining the time evolution of the radial profiles of the equatorial plasma mass density derived from field line resonances detected at the EMMA network (1.5 $<$ L $<$ 6.5). Finally, we presented the general features of the geomagnetic response to the CME, by applying innovative data analysis tools that allow to investigate the time variation of ground-based observations of the Earth's magnetic field during the associated geomagnetic storm.

Comprehensive Sun-to-Earth analysis of the Geoeffective Solar event of June 21, 2015: Effects on the Magnetosphere Plasmasphere Ionosphere system.

Mirko Piersanti[1,2] · Tommaso Alberti[3] ·

Alessandro Bemporad[4] · Francesco Berrilli[5] ·

Roberto Bruno[6] · Vincenzo Capparelli[7] ·

Vincenzo Carbone[3] · Giuseppe Consolini[6] ·

Alice Cristaldi[8] · Alfredo Del Corpo[1] ·

Dario Del Moro[5] · Simone Di Matteo[1,2] ·

Ilaria Ermolli[8] · Silvano Fineschi[4] ·

Fabio Giannattasio[6] · Fabrizio Giorgi[8] ·

Luca Giovannelli[5] · Salvatore

Luigi Guglielmino[7] · Monica Laurenza[6] ·

Fabio Lepreti[3] · Maria Federica Marcucci[6] ·

Matteo Martucci[5,9] · Matteo Mergè[5] ·

Ermanno Pietropaolo[1] · Paolo Romano[6] ·

Roberta Sparvoli[5] · Marco Stangalini[8] ·

Antonio Vecchio[10] · Massimo Vellante[1] ·

Umberto Villante[1,2] · Francesca Zuccarello[7] ·

B. Heilig[11] · J. Reda[12] · J. Lichtenberger[13]

Abstract A full-halo coronal mass ejection left the sun on June 21, 2015 from the active region NOAA 12371 encountering Earth on June 22, 2015, generating a G3 strong geomagnetic storm. The CME was associated with an M2 class flare observed at 01:42 UT, located near the center disk (N12E16). Using satellite data from solar, heliospheric, magnetospheric missions and ground-based instruments, we performed a comprehensive Sun-to-Earth analysis. In particular, we analyzed the active region evolution using ground-based and satellite instruments (BBSO, IRIS, HINODE, SDO/AIA, RHESSI – Halpha, EUV, UV, X), the AR magnetograms, using data from SDO HMI, the relative particle data, using PAMELA instruments and the effects of interplanetary perturbation on cosmic ray intensity. We also evaluated the 1-8 $\mathring{A}$ soft X-ray and low-frequency (~ 1 MHz) Type III radio burst time-integrated intensity (or fluence) of the flare in order to make a prediction of the associated Solar Energetic Particle (SEP) event by using the model developed by Laurenza *et al.* (2009). In addition, using ground based observations from lower to higher latitudes (INTERMAGNET EMMA, etc.), we reconstructed the ionospheric current system associated to the geomagnetic Sudden Commencement. Furthermore, SuperDARN measurements are used to image the global ionospheric polar convection during the SSC and

✉ Piersanti
mirko.piersanti@aquila.infn

1   Department of Physical and Chemical Sciences, University of L'Aquila, L'Aquila, Italy

3   Department of Physics, University of Calabria, Cosenza, Italy

5   Physics Department, University of Rome Torvergata, Rome, Italy

6   INAF-Istituto di Astrofisica e Planetologia Spaziali, Roma, Italy

7   Department of Physics and Astronomy, University of Catania, Catania, Italy

10   LESIA-Observatoire de Paris, 5 place Jules Janssen, 92190 Meudon, France

11   Geological and Geophysical Institute of Hungary, Tihany, Hungary

12   Institute of Geophysics-PAS, Warsaw, Belsk, Poland

8   INAF-Osservatorio Astronomico di Roma, Roma, Italy

4   INAF-Osservatorio Astrofisico di Torino, Turin, Italy

9   INFN, Laboratori Nazionali di Frascati, Frascati, Italy

2   Consorzio Area di Ricerca in Astrogeofisica, L'Aquila, Italy

13   Space Research Group, Department of Geophysics and Space Sciences, Eötvös University, Budapest, Hungary

during the principal phases of the geomagnetic storm. Moreover, we investigated the dynamics of the plasmasphere during the different phases of the geomagnetic storm by examining the time evolution of the radial profiles of the equatorial plasma mass density derived from field line resonances detected at the EMMA network (1.5 < L < 6.5). Finally, we presented the general features of the geomagnetic response to the CME, by applying innovative data analysis tools that allow to investigate the time variation of ground-based observations of the Earth's magnetic field during the associated geomagnetic storm.

1. Introduction

Coronal mass ejections (CMEs) are large-scale eruptions of plasma and magnetic fields from the Sun (Hundhausen, 1993). Nowadays, they are believed to be the main sources of the strong interplanetary disturbances (including shocks) that cause nonrecurrent geomagnetic storms (Sheeley *et al.*, 1985; Gosling *et al.*, 1990; Webb *et al.*, 2000; Zhang and Wang, 2002), playing a role in the largest recurrent storms as well (Crooker and Cliver, 1994; Crooker and McAllister, 1997). Geomagnetic storms (GS) are produced when mass and momentum are transferred from the solar wind (SW) into the magnetosphere. As a consequence, the magnetosphere falls in a strongly disturbed state, leading to intensification of the ring current (Daglis *et al.*, 1997) as well as of other current systems (i.e., Chapman-Ferraro current, Tail current and auroral electrojets (Dungey, 1961; Davis and Sugiura, 1966; Gonzalez *et al.*, 1994; Kamide and Kokubun, 1996; Consolini and De Michelis, 2005)). Frequently, a GS is accompanied by the injection of energetic electrons and ions into the inner magnetosphere (Li *et al.*, 2003). The strength of GSs is typically measured by the Dst index (Gonzalez *et al.*, 1994). Dst (measured in nT) is the hourly average of the deviations of the horizontal component of the magnetic field measured by several ground stations in mid and low latitudes. The effects of large magnetic storms can be seen both at ground and in near-Earth space. In fact, variations in the ionospheric and magnetospheric current systems (Villante and Piersanti, 2008, 2009) can ultimately create electric fields driving geomagnetically induced currents (Lanzerotti *et al.*, 2000). It has been fully established that the major single factor contributing to geoeffectiveness of CMEs is the existence of strong, long duration southward interplanetary magnetic field (IMF) component in some part of the ejecta or in the shear region ahead of the ejecta (Gonzalez *et al.*, 1994; Gonzalez, Tsurutani, and De Gonzalez, 1999). The physical mechanism for the SW energy transfer into the magnetosphere is the magnetic reconnection between the strong southward IMF and the northward dipole field of the Earth (Dungey, 1961).

High-energy particles, that originate from the Sun, mostly are in association with solar flares and/or CMEs. They consist of protons, electrons and lighter ions with energy ranging from a few tens of keV to a few GeV and are called Solar energetic particles (SEP). The mechanisms involved in the acceleration of SEPs are still unknown even if reconnection and rearrangement of magnetic field lines on the outermost layers of the Sun seem to play a central role. Moreover, SEP can be re-accelerated by the expanding CMEs; as these moves away from

the Sun they may be able to drive interplanetary shock waves that can accelerate again these particles (Reames (2013)). SEPs can be accelerated to energies of several tens of MeV within 5-10 solar radii (5% of the Sun-Earth distance) and can reach Earth in a few hours if the site of production on the Suns surface is magnetically connected to the Earth itself through the Parker spiral, reducing transport effects inside the heliosphere. Particularly energetic events,with particles exceeding the energy of 1 GeV, can cause showers of secondaries inside the atmosphere and can be detected on ground (these phenomena are called GLEs, Ground Level Enhancements). During GSs, SEP determines serious radiation hazard to astronauts and technological systems in space, influence the conditions in the ionosphere and thermosphere, cause enhancements of secondary cosmic rays and even contribute to the birth of new radiation belts (Lorentzen *et al.*, 2002; Valtonen, 2005).

In this paper, using data from solar, heliospheric, magnetospheric missions and ground-based instruments, we performed a comprehensive Sun-to-Earth analysis of the June 22, 2015 GS. In particular, we analyzed the active region evolution using ground-based and satellite instruments (BBSO, IRIS, HINODE, SDO/AIA, RHESSI – Halpha, EUV, UV, X), the AR magnetograms (SDO HMI), the early evolution in the lower corona of the solar eruption (SOHO/LASCO – VL), the relative particle data (PAMELA) and the effects of interplanetary perturbation on cosmic ray intensity. For this specific eruption no data were available from the STEREO mission, because the contact with the STEREO-B spacecraft was lost October 1st 2014, while IMPACT, PLASTIC, and SECCHI instruments on STEREO-A were turned off for superior solar conjunction from March 2015 until July 2015. We also tested the model developed by Laurenza *et al.* (2009) in order to make a prediction of the associated SEP event. In addition, we analyzed the response of the different magnetospheric current systems to the CME arrival by a comparison between TS05 model (Tsyganenko and Sitnov, 2005) predictions, magnetospheric observations and geomagnetic measurements during the Storm Sudden Commencement (SSC). In particular, using ground based observations from low to high latitudes, we reconstructed the ionospheric current system associated to the SSC. Moreover, we investigated the dynamics of the plasmasphere during the different phases of the geomagnetic storm by examining the time evolution of the radial profiles of the equatorial plasma mass density as inferred from field line resonances detected at the EMMA network (1.5 < L < 6.5). Moreover, we present the general features of the geomagnetic response to the CME, by applying innovative data analysis tools that allow to investigate the time variation of ground-based observations of the Earth's magnetic field during the associated geomagnetic storm and a description of the polar ionospheric convection is also presented. Finally, using SuperDARN measurements, we analyzed the polar ionospheric convection during the SSC and the principal phases of the geomagnetic storm.

2. Solar Data

The CME that encountered the Earth and generated the geomagnetic storm on June 22, 2015 was originated in active region (AR) NOAA 12371. This

Table 1. Characteristics of the two flares observed by the GOES-15 satellite in AR NOAA 12371, before the CME.

Flare	Class	Time (UT)		
		begin	peak	end
SOL2015-06-21T01:02	M2.0	01:02	01:42	02:00
SOL2015-06-21T02:06	M2.6	02:06	02:36	03:02

appeared on the eastern limb of the solar disk on June 16, 2015. At that time, its magnetic configuration was classified as β, evolving into $\beta\gamma\delta$ in the following days. On June 21 two subsequent flares were observed in the AR and their X-ray flux was measured by the GOES-15 satellite: SOL2015-06-21T01:02 and SOL2015-06-21T02:06, classified as M2.0 and M2.6, respectively. At 02:36 UT the SOHO satellite first observed the halo CME expanding into the heliosphere.

A number of solar facilities observed AR NOAA 12371 during its passage across the solar disk, and during time intervals close to the CME as well.

The Helioseismic and Magnetic Imager (HMI, Scherrer *et al.*, 2012) on board the Solar Dynamics Observatory (SDO, Pesnell, Thompson, and Chamberlin, 2012) took full-disk spectropolarimetric measurements in the Fe I line at 617.3 nm with a resolution of $1''$. The SDO/HMI data used in this work cover two days of observations, starting from June 20 at 00:10:25 UT until June 22 at 00:10:25 UT, with a cadence of 12 minutes.

In this analysis, we used SDO/HMI cylindrical equal area (CEA) Space-weather Active Region Patches (SHARPs) data (Hoeksema *et al.*, 2014). CEA SHARP data provide maps of the photospheric magnetic field of the AR projected and remapped to a cylindrical equal area Cartesian coordinate system centered on the tracked AR. Continuum intensity, Doppler velocity, and LOS magnetic field are also provided. We defer the reader to Bobra *et al.* (2014) for a comprehensive explanation of the SHARP pipeline. We selected a field-of-view (FOV) of these CEA SHARP data of about $476'' \times 228''$ encompassing the AR. Doppler measurements have been calibrated assuming umbral regions (i.e., with normalized continuum intensity < 0.4) at rest.

Furthermore, filtergrams acquired by the Atmospheric Imaging Assembly (AIA, Lemen *et al.*, 2011) aboard the SDO mission were used to study in detail the evolution of the flare in the coronal and upper chromospheric layers. We extracted a series of cutout images with a FOV that covers $515'' \times 388''$, also covering the FOV used for the CEA SHARP data. SDO/AIA cutouts are comprised in the time interval between 00:00 UT and 02:30 UT on June 21, with the highest available cadence (12 s for the EUV passbands, 24 s for the UV 1600 and 1700 Å images).

The spectropolarimeter (SOT/SP, Tsuneta *et al.*, 2008; Lites *et al.*, 2013) aboard the *Hinode* satellite (Kosugi *et al.*, 2007) acquired various raster scans over AR NOAA 12371, recording the Stokes profiles along the Fe I line pair at 630.15 nm and 630.25 nm. In particular, four scans were acquired with a pixel sampling of $0''.32$ and a polarimetric signal-to-noise ratio of about 10^3 (fast
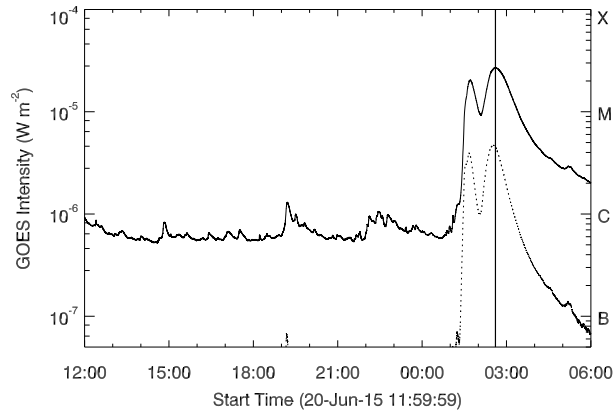
Figure 1. GOES flux curves in the 18 Å channel (solid line) and in the 0.54 Å channel (dotted line). The vertical line indicates the time of the first detection of the halo CME.

mode), starting at 14:47 UT and 19:41 UT on June 20 and at 00:37 UT and 06:11 UT on June 21. The first three scans covered a region of about $274'' \times 162''$, while the last scan cover only the central region of the AR with a FOV of $110'' \times 162''$.

The reconstructed SOT/SP continuum maps were aligned with the SDO/HMI continuum images closest in time, by using the IDL *SolarSoft* mapping routines. Level 2 data derived using the MERLIN inversion code (Lites *et al.*, 2007) were used in our analysis. We performed azimuth disambiguation of the Level 2 data using the non-potential magnetic field calculation technique (NPFC, Georgoulis, 2005), obtaining inclination and azimuth angles in the local solar frame.
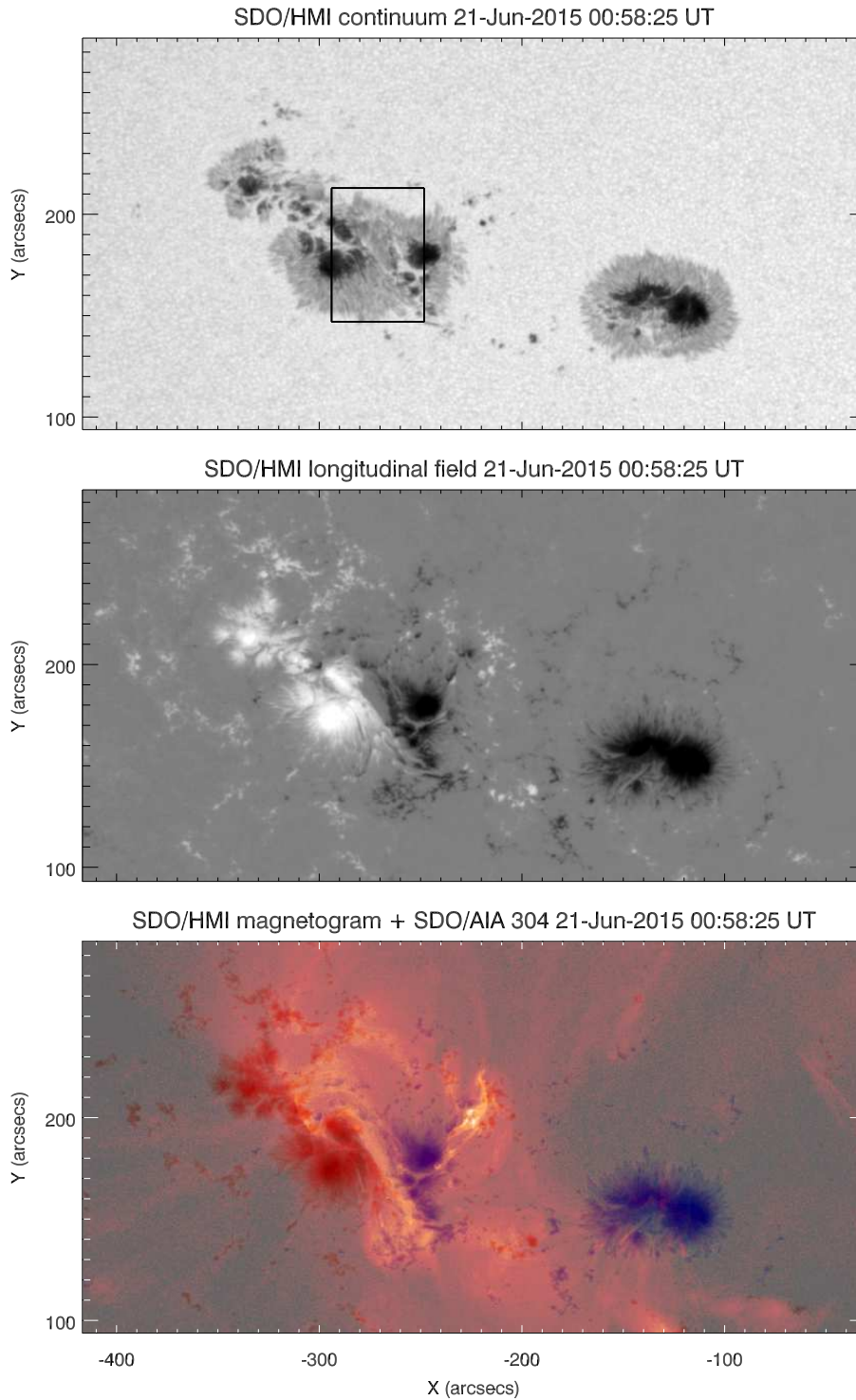
Figure 2. Top: Map of the photospheric continuum of AR NOAA 12371, acquired by SDO/HMI some minutes before `SOL2015-06-21T01:02`. The region indicated with a solid line shows the FOV used for the analysis of SOT/SP data. Middle: Simultaneous SDO/HMI magnetogram. The values of the longitudinal field are saturated at ±2000 G (white/black). Bottom: Simultaneous SDO/HMI magnetogram. Red (blue) areas indicate positive (negative) polarity. SDO/AIA emission at 304 Å passband is superimposed on the magnetogram map.

2.1. Solar trigger

In Figure 1 we plot the X-ray emission flux as measured by the GOES-15 satellite from 12:00 UT on June 20 until 06:00 UT on June 21. Two M-class flares are observed before the appearance of the halo CME. Their characteristics are resumed in Table 1. The first detection of the CME occurs near the peak of the second flare. Given this timing, we are not able to attribute the ejection to one or other of these flares. Such energetic events occurred after a rather long interval of low activity in the AR, as the previous flare (M1.0) occurred at 06:28 UT on June 20. Note that the C-class flare at around 19:00 UT on June 20 occurred in a different AR (NOAA 12367).

First, we analysed the large scale structuring of the AR 12371 and its eruptive potential, by estimating the fractal and multifractal properties of its photospheric configuration. Indeed, several studies in the literature indicate that measurements of such properties may help assessing, and even predicting, the flare activity of magnetic regions (for a list of studies carried out during the past decade see e.g. Ermolli *et al.* (2014)). Thus, we first explored the sensitivity of measurements of fractal and multifractal parameters on the eruptive activity observed for the AR 12371.

To this purpose, we analysed the time series of SDO/HMI CEA SHARP LOS magnetic field data described above. Following the data and methods applied in Giorgi *et al.* (2015) and Ermolli *et al.* (2014), we computed the fractal D_0 and D_8, and the multifractal Contribution Diversity C_{div} and Dimensional Diversity D_{div}, parameters on the subfield of about 256 arcsec × 256 arcsec centered on the AR.

Figure 3 shows the temporal evolution of the fractal D_0 and D_8 (top panels), and of the multifractal Contribution Diversity C_{div} and Dimensional Diversity D_{div} (bottom panels) parameters estimated for the studied region. In this figure, red (blue) symbols show the results of measurements carried out by considering the positive (negative) flux in the AR, while black symbols display the results of measurements from the unsigned magnetic flux data. Positive (negative) flux corresponds to trailing (leading) regions in the AR. Time 0 corresponds to 00:00 UT on June 20, 2015. Error bars indicate the standard deviation of the measured values as in Ermolli *et al.* (2014). For the sake of clarity, the deviation is only shown for the values derived from unsigned flux data. We also show the flaring activity of the AR 12371 over the analysed period. In each plot, the red-solid (violet-dashed) vertical lines indicate the time of occurrence of M-class (B- and C-class) flares. Flares associated with the CME occurred on June 21 2015 are indicated by thick line.

The studied region exhibits significant fractality, as the D_0 (D_8) values measured for its photospheric configuration range between ≈1.64 and ≈1.84 (≈1.52 and ≈ 1.72). With respect to the average and standard deviation of the parameters reported by Giorgi *et al.* (2015) for ARs hosting different flare classes, the values measured for the AR 12371 would have allowed to target it as likely M- and X-class flaring region ahead of the eruptive events observed on June 21, 2015. However, the trends in Fig. 3 seem to lack any further signature of the eruptive events hosted by the region. In agreement with results reported in the
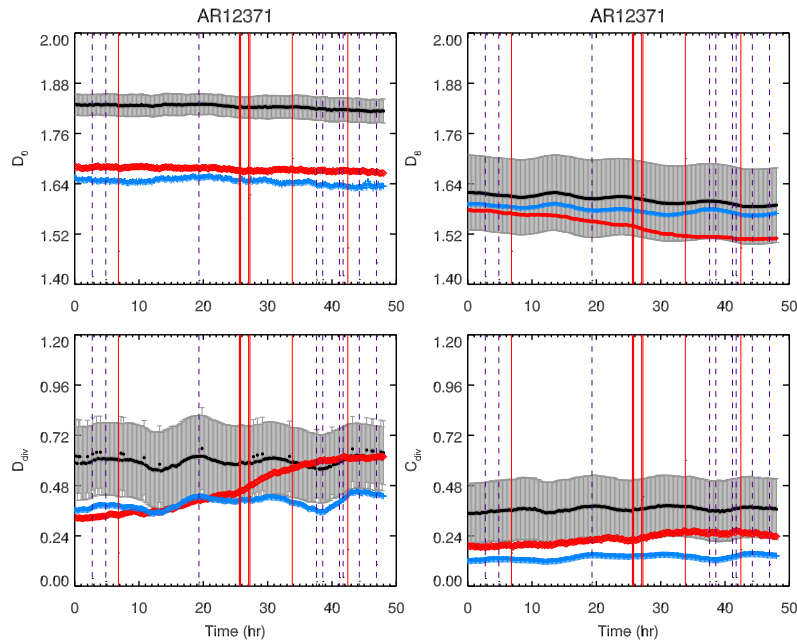
Figure 3. Time series of the fractal and multifractal parameters measured on the AR 12371, by considering both unsigned (black circles) and signed (positive and negative, red diamonds and blue crosses, respectively) flux data. Top: fractal parameters D_0 (left) and D_8 (right). Bottom: C_{div} (left) and D_{div} (right). Time 0 corresponds to 00:00 UT on June 20, 2015. Vertical red-solid (violet-dashed) lines indicate the time of occurrence of M-class (C-class) flares hosted by the AR. Flares associated with the CME occurred on June 21 2015 are indicated by thick line. Error bars show the uncertainty associated with the measured values, details are given in the text. For clarity, the error bars are only shown for the results from unsigned flux data.

literature, the fractal and multifractal parameters estimated for the region have opposite temporal evolution. Indeed, the time series of the fractal (multifractal) parameters measured on the AR 12371 look rather similar and flat over time, but for the results of the D_0 and D_8 (C_{div} and D_{div}) measurements derived from the positive flux data that show a net decrease (increase) during the analyzed period. The trends of the values estimated for the same quantities from unsigned and negative flux data are rather unvaried over time. We conclude that, while the above measurements point out the eruptive potential of the AR 12371 ahead of the events occurred on June 21, 2015, they also suggest the lack of clear effects of these events in the photospheric configuration of the AR 12371 magnetic field.

Figure 2 (top panel) shows the photospheric configuration of AR NOAA 12371, a few minutes before the start of `SOL2015-06-21T01:02`. The AR exhibited a central part with opposite polarities in contact to each other, sharing some penumbral filaments (δ configuration, see Figure 2, middle panel). At chromospheric heights, a sigmoidal-like structure is visible along the polarity inversion line (PIL) present in the region (bottom panel).

Along the PIL, there are found peculiar flows of upflows/downflows of about ∓ 1.5 km s^{-1}, which are not related to the classical Evershed flow observed in sunspots. These flows are reminiscent of the velocity field configuration found

in δ complexes by Cristaldi *et al.* (2014), which has been attributed to shear accumulation.
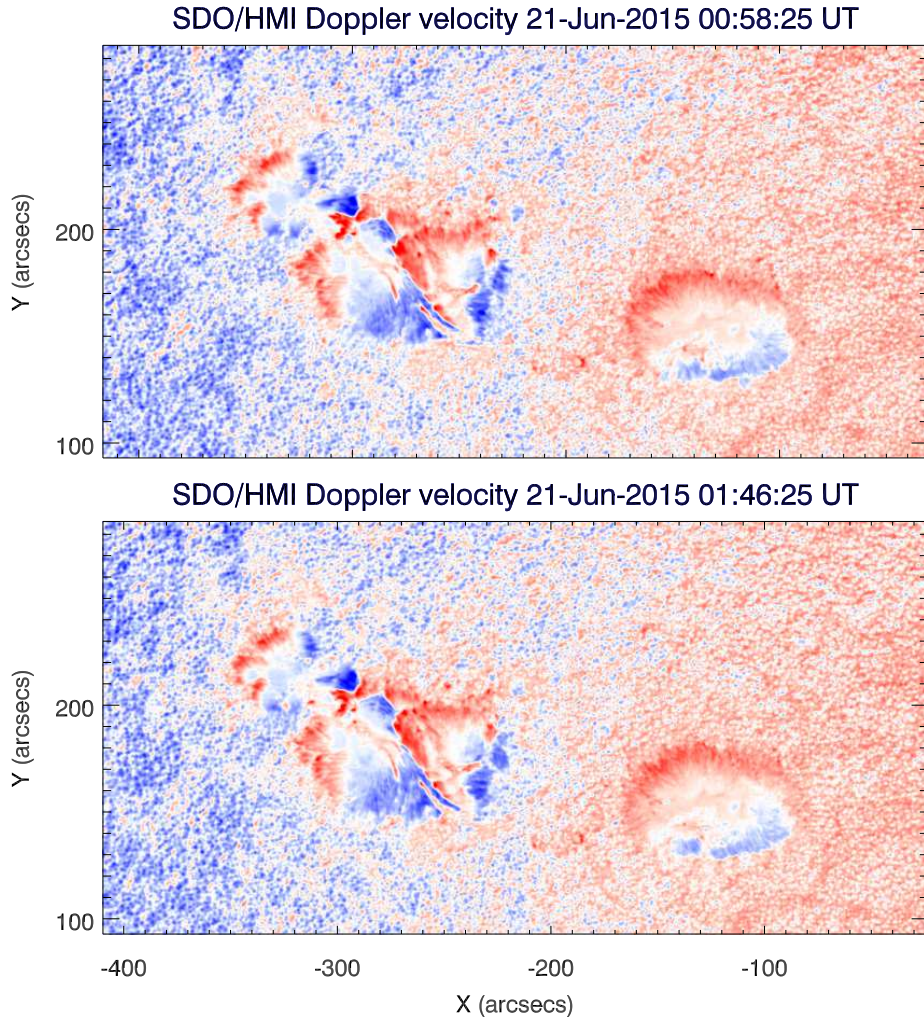

Figure 4. Top: Map of the Doppler velocity of AR NOAA 12371, acquired by SDO/HMI some minutes before `SOL2015-06-21T01:02`. Bottom: Same at the time of flare peak. The values of the Doppler velocity are saturated at ∓ 1.5 km s^{-1} (blue/red).

In Fig. 5 (*left*) we show a continuum HMI image reporting the photospheric configuration of AR NOAA 12371 with overlapped a red box indicating the IRIS satellite FoV, while the blue box indicates the BBSO FoV centered in the δ complex. Fig. 5 (*right*) shows an image acquired by BBSO in the wing of the TiO line, which shows the details of the δ complex. We can see that the eastern umbra is characterized by the presence of light bridges and that the penumbral filaments located between the two opposite polarity umbrae are highly sheared.
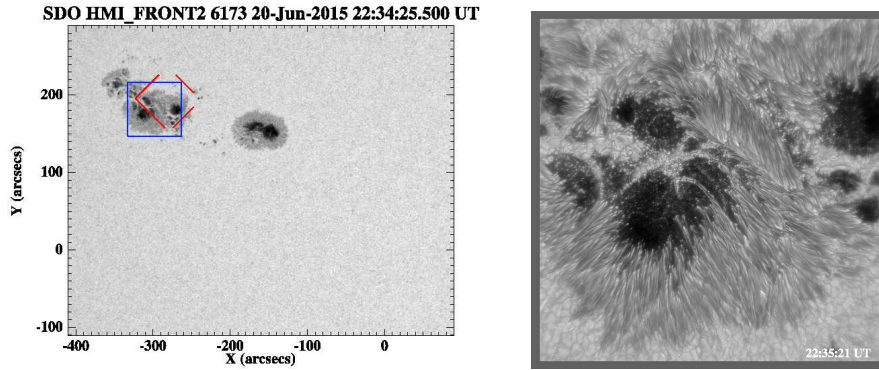
Figure 5. Left: continuum SDO/HMI image showing the photospheric configuration of AR NOAA 12371. The red box indicates the FoV observed by the IRIS satellite; right: BBSO image acquired in the wing of the TiO line.
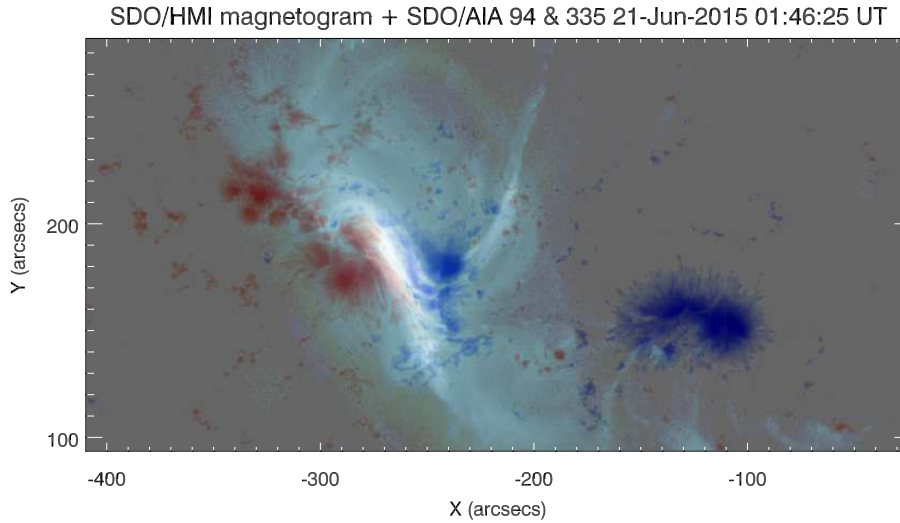

Figure 6. SDO/HMI magnetogram at the peak of `SOL2015-06-21T01:02`. Red (blue) areas indicate positive (negative) polarity. A composite image of SDO/AIA emission at 94 Å and 335 Å passbands is superimposed on the magnetogram map.

The M2.0 flare is located along the PIL, as shown in Figure 6. Figure 7 displays the morphology of the coronal regions of AR NOAA 12371 close to the flare peak, as visible in SDO/AIA images. The online movies in the various passbands show that, actually, the evolution between the two M2.0 and M2.6 flares occurs without interruption. During the event, several coronal structures are destabilized in a succession reminiscent of a domino-like effect (e.g., Zuccarello *et al.*, 2009), triggered by an activation process occurring in the δ complex. In this sense, `SOL2015-06-21T01:02` and `SOL2015-06-21T02:06` can be considered a unique event.
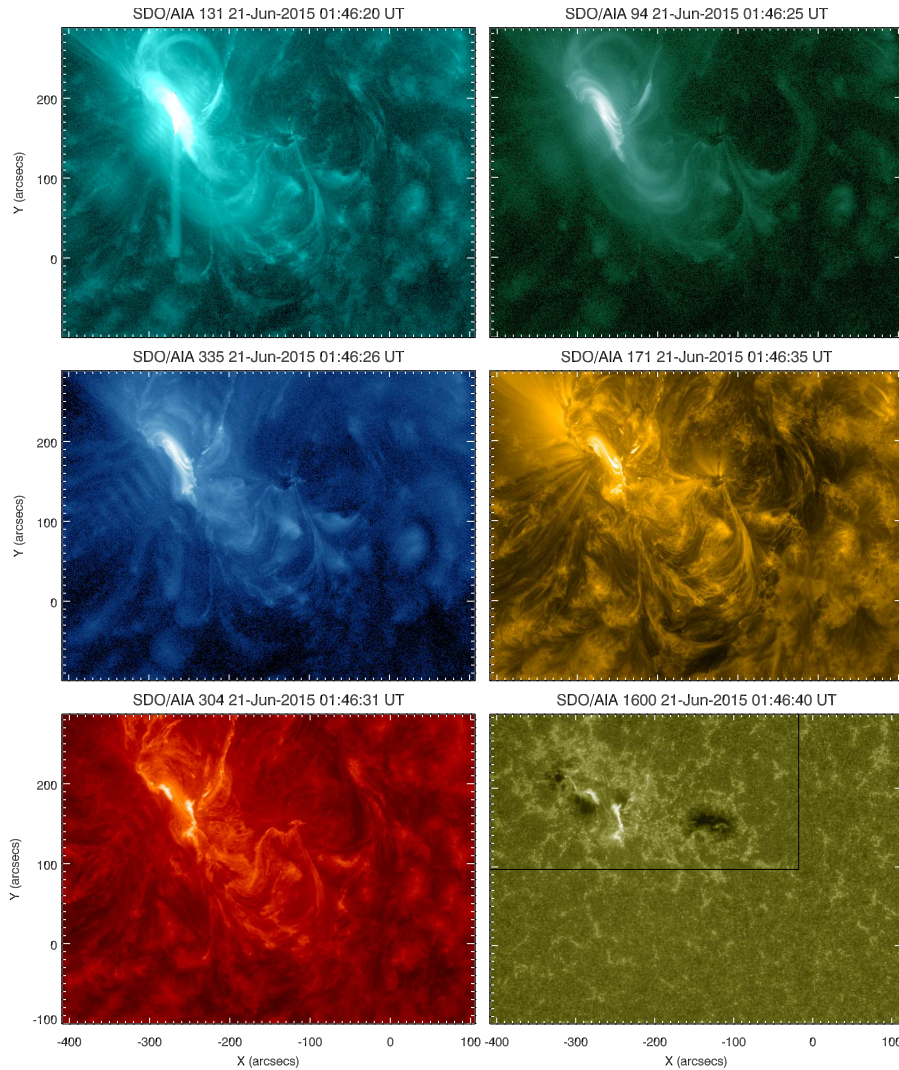
Figure 7. Morphology of AR NOAA 12371 at the peak of `SOL2015-06-21T01:02`. The rectangle in the 1600 Å map indicates the FOV shown in Figure 6 as a reference. An animation of this figure is available in the online journal.

In particular, Figs. 8 and 9 show the evolution of the event at two different atmospheric heights, as deduced from AIA 211 Å and 304 Å images, respectively. We can see that the event, triggered in the region hosting the δ sunspot, involves also locations quite far from this sunspot (see, e.g. at coordinates [-200:-100], [-50:50]), where it is possible to recognize the signatures of a filament activation and eruption. As these images show, the size of the region involved is quite large, implying a considerable amount of mass which could be ejected and be later observed as a coronal mass ejection.
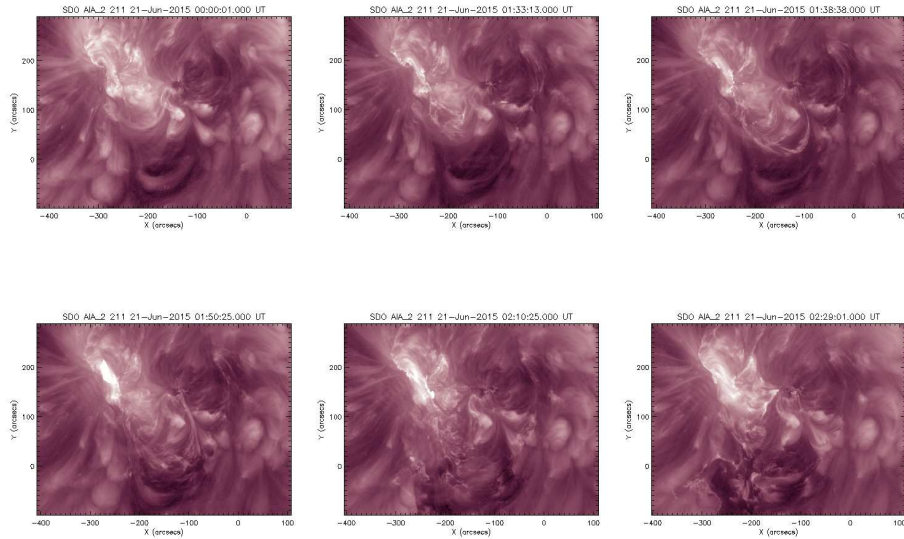
Figure 8. Sequence of AIA 211 Å images showing the evolution of the flare occurred in NOAA 12371. The two ribbons of the flare are clearly visible at [-300:-180], [80:300] in all the images. The destabilization and later eruption of a filament can be observed starting at 01:38 UT at coordinates [-200:-100], [-50:50]. An animation of this figure is available in the online journal.

To investigate the configuration of the coronal magnetic field of the NOAA 12371 at coronal levels, we used a linear force-free extrapolation code based on a method introduced by Alissandrakis (1981). The model assumes that the magnetic field is force-free both in the corona and at lower levels, and vanishes at infinity. We used as input parameters the values of the longitudinal magnetic field component at the boundary (i.e. the photosphere), provided by SDO/HMI at 00:58:25 UT. We used a force-free parameter equal to -0.01 pixel^{-1} to reconstruct the coronal magnetic field configuration and obtains the values of each component of the magnetic field in 3D space. The result is shown in Figure 10, where we distinguish the main flux tubes involved in the event. The blue field lines seems to reproduce quite well the brightest loops visible in Figure 6. We also distinguish the overlying arcade which has been involved in this solar eruption.

In order to provide a global view of the magnetic field configuration of the whole Sun, we also outlined the magnetic configuration of the corona by extrapolating the coronal magnetic field lines according to the model developed by Schrijver and DeRosa (2003); employed in the SolarSoft package called the Potential Field Source Surface (PFSS)). The coronal magnetic field is extrapolated from the photospheric field via the PFSS approximation, in which the field is assumed potential in the coronal volume between the photosphere and a spherical source surface of 2.5 solar radii. Since the coronal field models are provided at a 6 hr cadence by the online database of PFSS, Figure 11 shows the
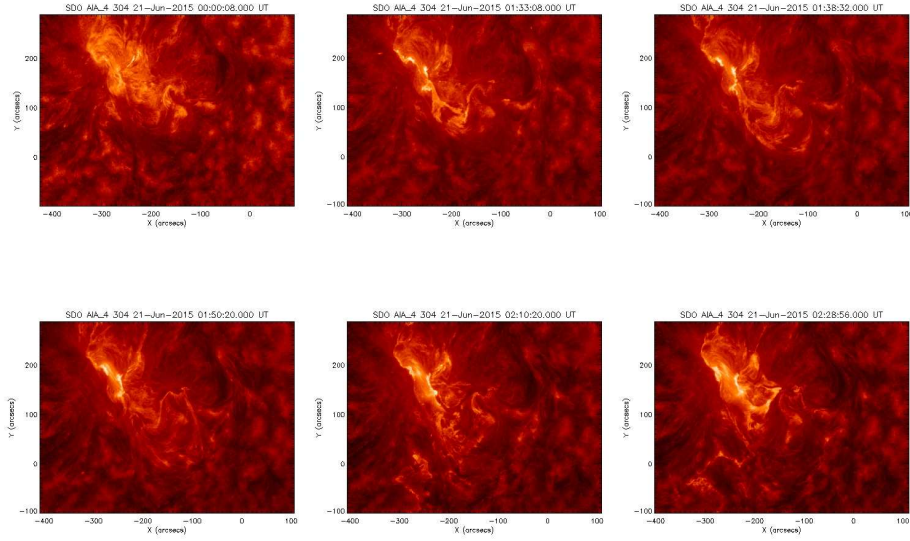
Figure 9. The same as in Fig. 8, but for a lower atmospheric level, as observed by AIA at 304 Å. An animation of this figure is available in the online journal.

magnetic configuration closest in time to the beginning of the flare, 1.e. 2015 June 21 at 00:04 UT. The extrapolations have been generated while taking into account the Earth line of sight. We note several open magnetic field lines around the NOAA 12371 and directed towards the Earth (indicated in green in Figure 11).
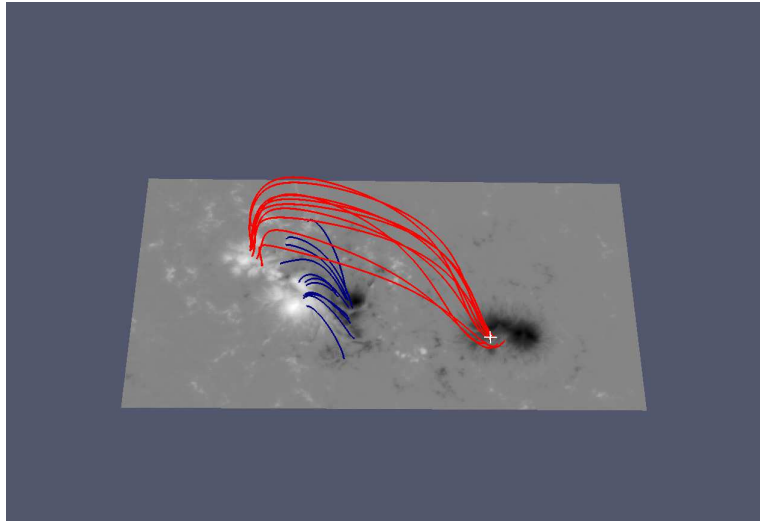
Figure 10. Linear force free extrapolation of the photospheric magnetic field of the AR NOAA 12371.
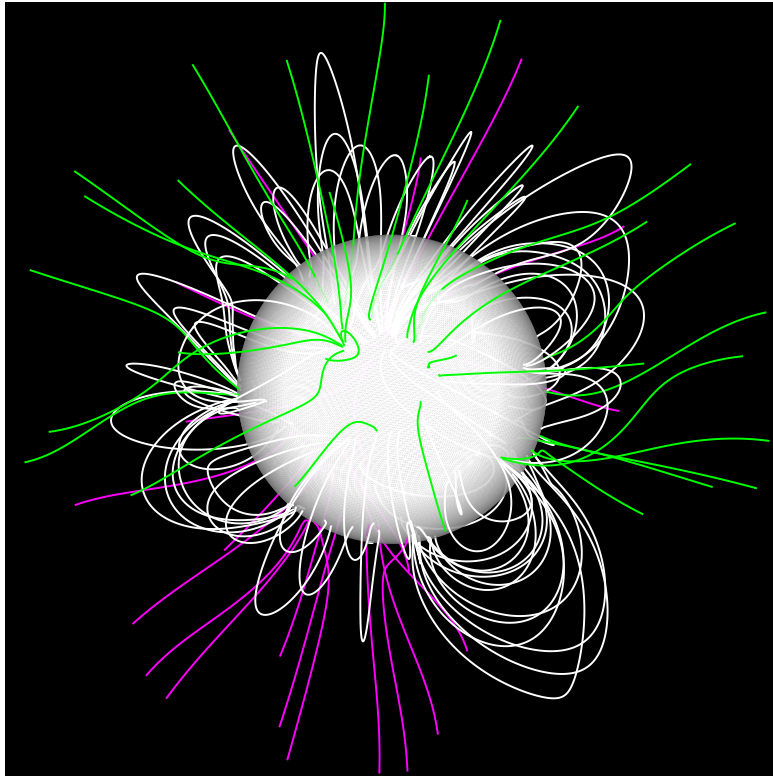
Figure 11. Potential field extrapolation of the full disk magnetic field on June 21 at 00:04 UT.

The subFOV $110'' \times 162''$ indicated with a solid line in Figure 2, which corresponds to the PIL region, was observed during all of four SOT/SP raster scans. Figure 12 (left panel) shows the vertical component of the solar magnetic field (Bs_z) in this region. The red line indicates the strong PIL, i.e., the region where Bs_z changes sign and Bs_t (the transverse component) is stronger than 500 G.

We estimated the shear between the observed (measured) horizontal field and the horizontal field derived through a potential field extrapolation (Wang *et al.*, 1994), according to Falconer, Moore, and Gary (2002) and Jiang *et al.* (2016). The potential field was computed using the method described by Alissandrakis (1981). As a proxy of this shear, we used the horizontal shear angle θ, as defined in Romano *et al.* (2014); Gosain and Venkatakrishnan (2010).

We computed the dip angle, which measures the difference between the inclination angle of the observed field and that of the potential field (see, e.g., Gosain and Venkatakrishnan, 2010; Petrie, 2012; Romano *et al.*, 2014). This quantity is defined as

$$\Delta\gamma = \gamma^{\mathrm{obs}} - \gamma^{\mathrm{pot}} \tag{1}$$

where $\gamma = 90° - \arctan(Bs_z/Bs_t)$ is the inclination angle derived in both cases.

Table 2. Evolution of the mean value of shear angle θ, dip angle $\Delta\gamma$, current $|j_z|$, and gradient $|\nabla Bs_z|$, along the PIL of AR NOAA 12371.

Time (UT)	$<\theta>$ (degrees)	$<\Delta\gamma>$ (degrees)	$<|j_z|>$ (mA/m^2)	$<|\nabla Bs_z|>$ (G/m)
2015-06-20 15:10:48	42.7	0.94	16.0	14.4
2015-06-20 20:03:52	43.9	-2.19	17.9	25.2
2015-06-21 01:00:29	67.6	-1.23	18.2	12.4
2015-06-21 06:22:26	64.1	-0.93	13.4	9.8
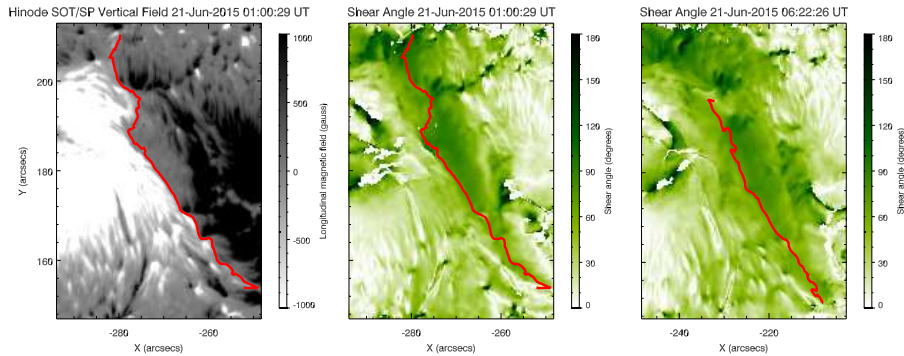
Figure 12. Maps of the vertical component Bs_z some minutes before the start of the flaring activity in AR NOAA 12371 (left), a simultaneous map the shear angle (middle), and a map of the shear angle three hours after the flares (right). The solid red line indicates the PIL.

The resulting maps of shear angle are shown in Figure 12, just a few minutes before the M2.0 flare (middle panel) and after some hours (right panel).

We can see that the region between the opposite polarities of the δ complex underlying the filament seen in the SDO/AIA 304 passband is characterized by high values of the shear angle, larger than 45°. Note that small patches in the FOV far from the PIL showing a large shear angle, near regions with Bs_t less than 200 G (white background) may be affected by errors in the 180° azimuth ambiguity resolution. The shear angle exhibits a slight decrease after the flare.

We also used the results obtained with the NPFC code to estimate the electric current in the vertical direction, $|j_z|$, and the gradient of the vertical component of the magnetic field, $|\nabla Bs_z|$, following Georgoulis and LaBonte (2004).

In Table 2 we report the mean (unsigned) values of the shear angle, dip angle, $|j_z|$, and $|\nabla Bs_z|$ calculated along the PIL. We see that the shear angle increases until the flares occur, and decreases at the end. The dip angle exhibits a similar behavior. Also $|j_z|$ values grow until the eruptive event occurs and diminish after the flares, while $|\nabla Bs_z|$ begins to lessen before the events. This trend indicates that a dynamical process of energy storage is taking place during hours before the eruptive phenomena, through shear accumulation. Then, after the energy release events, a relaxed state is reached.

## 3. Flare forecasting parameters from SDO/HMI magnetograms

A variety of magnetic field proxies is used to characterize Active Regions (ARs) and to try to forecast flaring events occurrence, see e.g. Falconer, Moore, and Gary (2002); Leka and Barnes (2003, 2007); Schrijver (2009). In this section we concentrate on 4 variables which have been proved to provide a statistical forecast estimation of flares: log(R), TOTUSJZ, TOTUSJH and TOTPOT.

The log(R) parameter is a measure of the unsigned flux near the magnetic polarity separation lines. The log(R) is a proxy of the photospheric electrical currents introduced in Schrijver (2007) and is a measure of the maximum energy available in the AR. Using a vast dataset from MDI, probability of flare occurrence given a certain log(R) value has been established. The TOTUSJZ, TOTUSJH and TOTPOT are respectively the total unsigned vertical current, the total unsigned current helicity and the total photospheric magnetic energy. We choose these parameters as they have high scores in a machine learning based algorithm which use a vast statistics of HMI data to derive flaring ARs, see Bobra and Couvidat (2015).

We retrieved the time series of the four magnetic parameters from the HMI data repository, located at the Joint Science Operations Center. In particular, we used the SHARP data (see Bobra *et al.* (2014)), which calculate the selected parameters with a 12 minutes cadence on the whole AR region.

We report in the plots (see figures 13 to 18) the time evolution of the four parameters for NOAA AR12371, spanning from June 15 (AR emerging from east limb) to June 26. We mark in yellow the portion of the dataset with a solar longitude > 60°, which should be disregarded due to projection effects. We report as shaded grey areas the time spanning of the flares produced by AR12371 only and in red the M2 flare which produced the full-halo CME we are investigating. The intensity of the flare is marked on the plot at the flare peak intensity position.

We notice from figure 13 that the log(R) value, and therefore the probability of having an M flare, is high for the whole period. We remark here that, while the log(r) values are based on HMI magnetograms, the occurrence rates of M- or X-class flares for a given log(R) value have been computed on MDI data and are therefore only indicative. A new calibration is necessary to calculate the exact conditional flare probabilities based on HMI magnetograms. In any case, the flare prediction is in good agreement with the observed sequence of 6 M-class flares, spanning up to an M7.9. The flare sequence starts with an M3 while the log(R) is still rising but already with a high value. After a peak on June 19 the log(R) begin to lower while the flares release magnetic energy from AR12371. As visible also in the plots in figures from 17 to 18, which are in qualitative agreement with the log(R) values, the eruptive potential of the ARAR12371 remains high for the whole period taken into account, the trend over 24h has a minor decrease well after the flare eruption. In particular, the zoom on the log(R) value close to the flare event plotted in Figure 14 shows that the flare probability stays the same after the event, with a similar behaviour as those reported in figure 3 for the
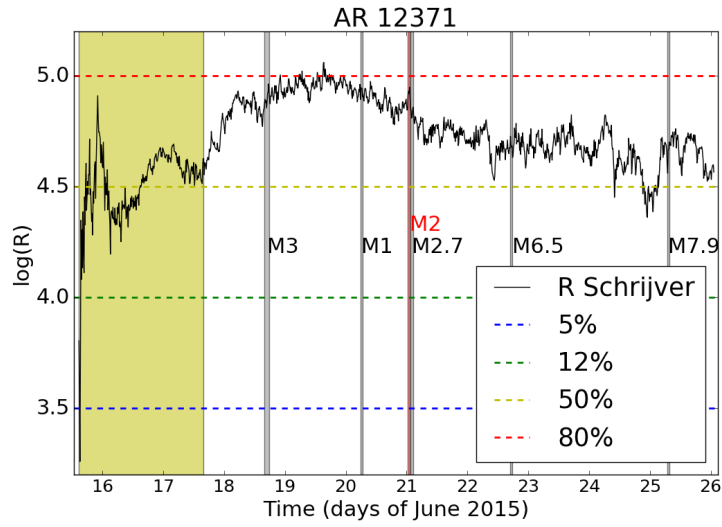
Figure 13. The log(R) parameter as a function of time. We report the probability to have a flare > M1 in the next 24 hours as from Schrijver (2007). Shaded yellow area: solar longitude > 60°. Shaded grey and red: flares > M1 produced by AR12371.
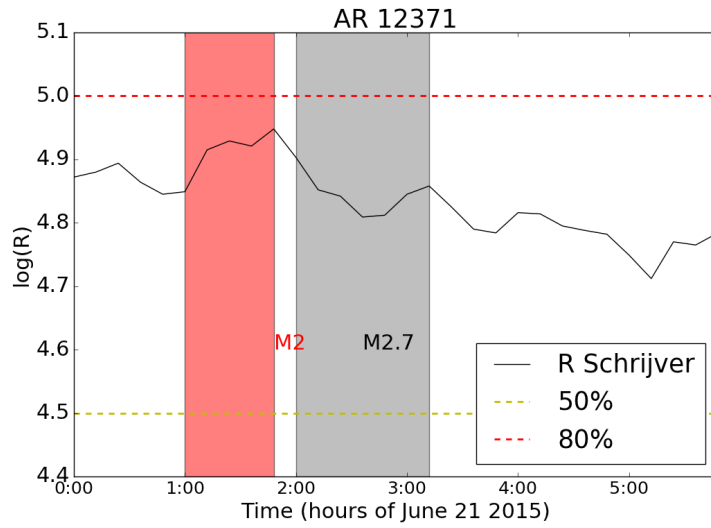
Figure 14. The log(R) parameter as a function of time. We here concentrate on the first hours of June 21 2015. We report the probability to have a flare > M1 in the next 24 hours as from Schrijver (2007). Shaded areas: flares > M1 produced by AR12371, in red the flare investigated in this paper.
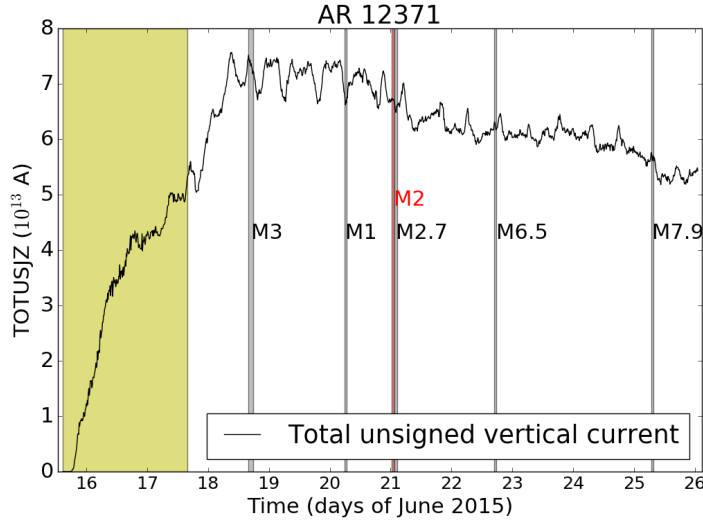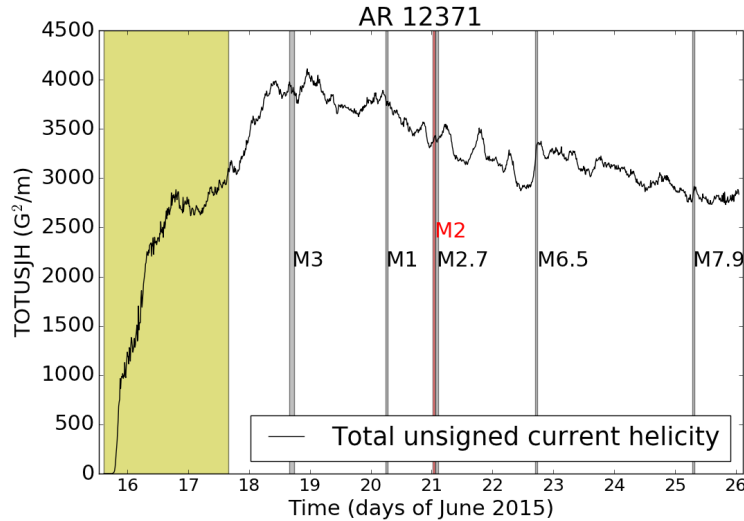
Figure 15. The total unsigned vertical current as a function of time. Shaded yellow area: solar longitude $> 60°$. Shaded grey and red: flares $> M1$ produced by AR12371.

multifractal parameters. This supports the conclusions reported in section 2.1, stating that there is little or no evidence at all of a change of configuration of the magnetic field at photospheric level associated to the flare.

4. Halo CME

As we mentioned, during the June 21, 2015 event none of the space-based coronagraphs on-board STEREO spacecraft was acquiring data. Nevertheless, the LASCO-C2 and -C3 visible light coronagraphs on-board SOHO acquired a very nice sequence of images showing the halo-CME and the CME-driven shock expanding towards the Earth. In particular during the event the LASCO-C2 coronagraph (with a projected field of view going from 2.1 to 6.0 solar radii) acquired images with the "Open" filter at 02:36 UT (the last frame just before the CME enters in the LASCO-C2 field of view) and at 02:48, 03:12, 03:24 and 03:36 UT. This sequence shows nicely the early expansion of the halo-CME, as well as the propagation of the CME-driven shock ahead of the CME front. The subsequent expansion of the CME was captured higher up by the LASCO-C3 coronagraph (with a projected field of view going from 3.6 to 33 solar radii), that acquired images with the "Open" filter at 03:06 UT (the last frame just before the CME enters in the LASCO-C3 field of view) and at 03:18, 03:12, 03:24 and 03:36 UT. This sequence shows very well the interplanetary expansion of the halo-CME.

By using standard LASCO running difference sequences, this event has been preliminarily analyzed in different automatic and semi-automatic CME catalogues, such as the SEED, CACTUS, CORIMP, and CDAW catalogues available
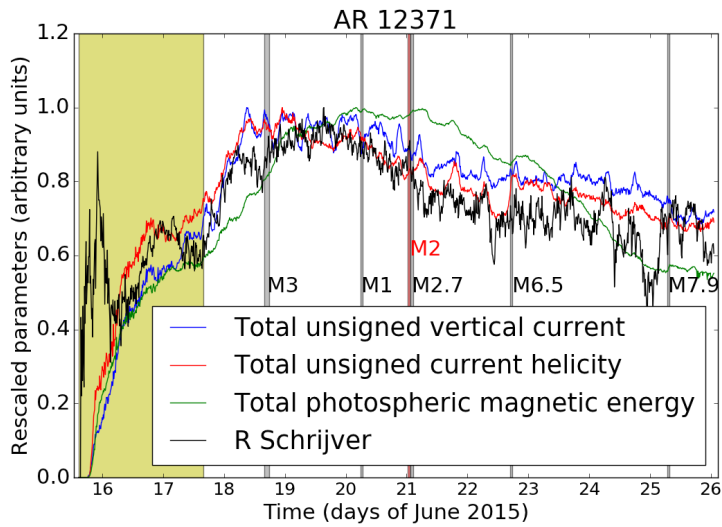
Figure 16. The total unsigned current helicity as a function of time. Shaded yellow area: solar longitude $> 60°$. Shaded grey and red: flares $> M1$ produced by AR12371.

on-line. In particular, the SEED catalogue gives on average (after linear fitting of automatic determination of the CME front location in two LASCO-C2 frames) a projected plane of the sky speed of 1009 km s^{-1}. The other two catalogues provide broad and quite complex velocity distributions depending on the considered feature along the expanding CME front. The CACTUS catalogue divided the event into two partial-halo fronts and provided median velocities of (980 ± 300) km s^{-1} and (840 ± 300) km s^{-1} for the upper and lower half of the halo-CME front, while the CORIMP catalogue provides nice filtered LASCO-C2 and C3 composite movies of the event, as well as time-distance, time-velocity, and time-acceleration curves for different position angles along the CME front. According to the CORIMP catalogue the CME is slightly accelerating ($a \simeq 150$ m s^{-2}) during the early expansion phase (between ~ 3 and ~ 6 UT), and then slightly decelerating ($a \simeq -150$ m s^{-2}) higher up in the LASCO-C3 field-of-view. This result in a projected speed going up to $\sim 600 - 1100$ km s^{-1} around ~ 6 UT and then progressively decreasing down to a terminal speed between $\sim 200 - 500$ km s^{-1}. The CDAW catalogue estimates (with linear fitting of the CME front location in LASCO-C2 and -C3 images) a CME starting time at 02:06:49 UT, hence in very good agreement with the occurrence of the M2.6 class flare.

Very interestingly, the LASCO-C2 instrument acquired a polarized sequence just at the right time when the CME front crossed the instrument field of view. In particular, the 3 images of the polarized sequence were acquired at 02:54:08 UT (polarization angle +60 degree), 02:57:58 UT (polarization angle 0 degree) and 03:01:48 UT (polarization angle -60 degree). Moreover, another polarized sequence was acquired just a few hours before the CME, and in particular on June 20 at 21:00:03 UT (polarization angle +60 degree), 21:03:53 UT (polarization angle 0 degree) and 21:07:43 UT (polarization angle -60 degree). All these
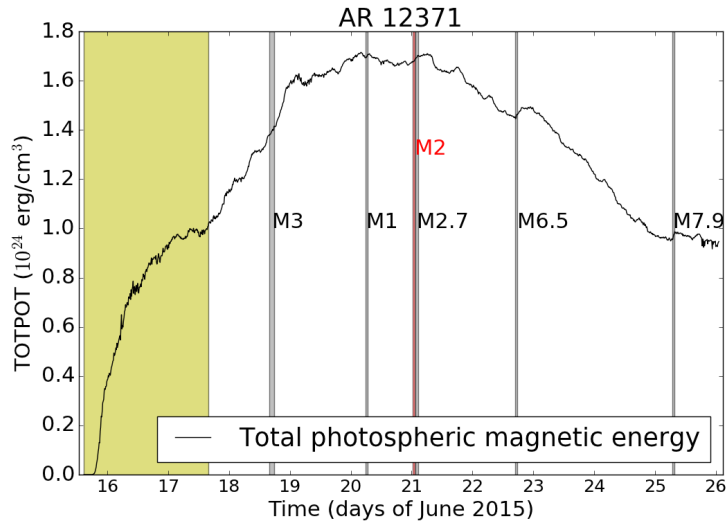
Figure 17. The total photospheric magnetic energy as a function of time. Shaded yellow area: solar longitude $> 60°$. Shaded grey and red: flares $> M1$ produced by AR12371.


Figure 18. Rescaled parameters as a function of time. We rescale to unity all the parameters in order to compare the trends. Shaded yellow area: solar longitude $> 60°$. Shaded grey and red: flares $> M1$ produced by AR12371.
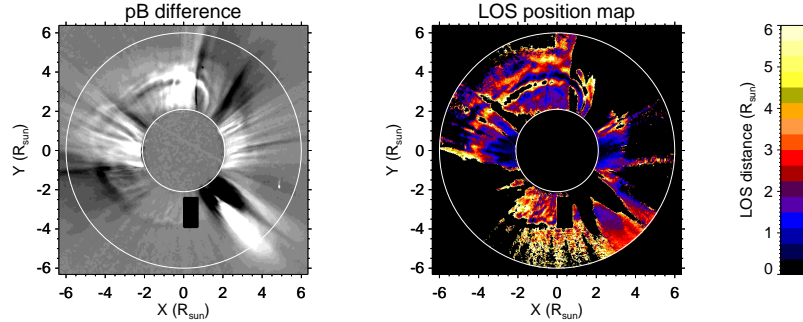
Figure 19. Left panel: the difference between the pB image acquired during the halo CME (polarized sequence acquired on June 21 between 02:54 and 03:02 UT) and the last pB image available before the eruption (polarized sequence acquired on June 20 between 21:00 and 21:08 UT). Negative values (black) have been excluded in the polarization ratio analysis to consider only pixels (white) where the CME transit leads to a density increase. Right panel: map of the position along the LOS of the density increases associated with the CME as obtained with polarzation ratio technique (see text).

images, with size by 512×512 pixels, were acquired with an exposure time by 100 s. This allowed us to perform the polarization ratio analysis on this event and to determine the 3D distribution of the emitting plasma. As it was first pointed out by Moran and Davila (2004), because of the Thomson scattering geometry, for a single electron the ratio between the polarized (pB) and unpolarized (uB) white light brightness is dependent only on its location along the line of sight z. For any coronal feature, the ratio pB/uB has a more complex dependence on the distribution of the electron density integrated along the line of sight (Bemporad and Pagano, 2015), and the possibility that the feature is located near the plane of the sky makes the interpretation of results more complex. On the other hand, for a halo CMEs the computation has some simplifications, because the emitting CME plasma is located almost entirely ahead or behind the plane of the sky. In our analysis we first derived base difference pB and uB images (see Figure 19, left panel) neglecting all the pixels where the difference was negative, in order to isolate only those pixels where additional emission due to the CME expansion and/or compression is present. Then, from the observed pB/uB ratio we determined with the standard technique described by Moran and Davila (2004) the location z of the emitting plasma along the line of sight.

The resulting map of z values is shown in Figure 19 (right panel); this map suggests a correlation between distances ρ from the Sun projected on the plane of the sky and distances z along the line of sight, indicating that the reconstructed
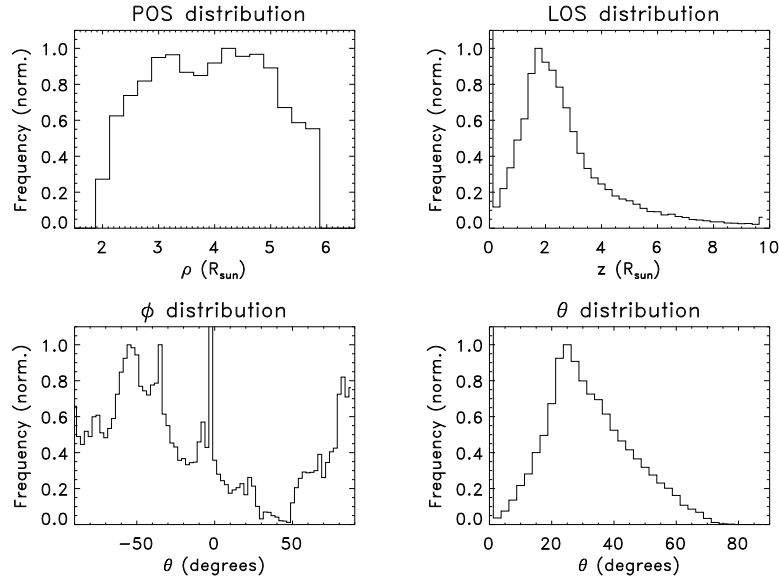
Figure 20. bar-plots showing the distributions (as obtained from polarization ratio) in analyzed pixels of the emitting plasma location on the POS (top left), along the LOS (top right), of the latitude angles ϕ of those points (bottom left) and of their angles with respect to the POS (bottom right).

cloud of 3D points has a distribution similar to the surface of a cone with vertex located on the CME source region on the Sun and axis parallel to the line of sight. In order to better understand the resulting 3D structure of the halo CME, we built bar-plots (Figure 20) showing the distribution of POS distances ρ (top left panel), LOS distances z (top right), as well as the distribution of polar angles ϕ on the POS (bottom left) and of angles θ from the POS. These plots show that points where the polarization ratio technique is successful are distributed quite homogeneously in projected distance on the POS and less homogeneously in polar angle; moreover, the bulk of reconstructed points is located at a distance of about 2 solar radii from the POS and that are expanding at an angle from that plane of about $25°$. We point out that a big source of uncertainty is related with the total time required to acquire the whole polarized sequence by about 7m 20s; during this time any CME feature with projected speed of 1000 km s^{-1} moved by ~ 600 arcsecs, corresponding to ~ 25 pixels (for a 512×512 pixels LASCO-C2 image).

All the above information derived from white light images are crucial to predict the CME arrival time at 1 AU and to study the CME interplanetary propagation. For instance, a simple estimate of the Interplanetary CME (ICME) arrival time at 1 AU can be determined by using the on-line forecasting tool provided by the Hvar Observatory (http://oh.geof.unizg.hr/DBM/dbm.php). The tool runs a 1D drag-based model , given some input parameters. In particular we can assume that (as provided by the CORIMP catalogue) the CME was at a projected altitude of 25 solar radii on June 21 around 08:00 UT with a projected

speed around 300 km s^{-1}. These quantities can be deprojected by using the propagation angle of 25° from the plane of the sky as we determined for the halo-CME front: in this way we estimate that on June 21, 08:00 UT the CME front was at a de-projected altitude of $25R_{sun}/\cos 25° \simeq 27.6R_{sun}$ with a de-projected speed of 330 km s^{-1}. With these input parameters, by also assuming a background solar wind speed of 400 km s^{-1} as measured by ACE spacecraft in the days before the eruption, the propagation tool provides an estimated arrival time on June 25, 19:04 UT (by assuming the smallest allowed value for the drag parameter of $\Gamma = 0.1 \times 10^{-7}$ km^{-1}). This is much later than the observed arrival time of the interplanetary shock. In particular, ACE observed the arrival of the shock on June 22, $\sim$ 18 UT. This early arrival time can be reproduced by the drag-based model only by assuming (again with the smallest allowed value for the drag parameter) an initial speed at 1 solar radius equal to 1440 km s^{-1}; this very high velocity is likely compatible only with the shock propagation velocity.

5. The 21 June 2015 Solar energetic particle (SEP) event

A SEP event was observed on 21 June 2015, which can be associated with the M2.6 flare (peak time on June 21 at 02:36 UT) occurring in the active region 12371, located at N13W00, and the concomitant full halo CME at 02:36 UT. This SEP event was also accompanied by Type II and Type IV radio sweeps, indicating the presence of a propagating interplanetary shock, and Type III radio signatures.

At geosynchronous orbit, the particle instrument (EPAD) of the Geostationary Operational Environmental Satellites (GOES) recorded an increase in the proton and electron fluxes. The top panel of Figure 21 shows the flux profiles for protons of energies > 10, > 30 and > 60 MeV. The observed proton fluxes at all of the energy channels show a gradual rise in the prompt phase (as expected for a central meridian event) and a maximum value. On the other hand, the following decrease is quite slow at > 10 MeV and sharp at high energies (> 30 and > 60 MeV). Specifically, the >10 MeV proton flux crossed the 10 pfu threshold (i. e., start of the SEP event according to the NOAA definition) at 21:35 UT on 21 June, reached the maximum flux value of 1070 pfu at 19:00 UT on 22 June and fell below 10 pfu (end of the SEP event) at 07:05 UT on 24 June. The observed enhancement around the peak value at 19:00 UT (on 22 June), which reaches the strong radiation level (S3, according to the NOAA definition) is due to a shock arrival at the Earth. As a matter of fact, at 17:59 UT (vertical black line in Figure 21) on 22 June, a shock was observed in ACE solar wind and magnetic field data (18:07 UT at WIND), driven by the 21 June CME, and a storm sudden commencement (SSC) was registered at 18:37 UT at the Earth (see section 7.1). In addition, the enhancement around the proton flux local peak at 11:00 UT on 22 June could be the effect of a small shock (related to a previous CME on 19 June), which was observed at 04:51 UT (vertical dashed black line in Figure 21) at the ACE spacecraft location, followed by a geomagnetic sudden impulse (SI) at 05:49 UT. Note that the 21 June 2015 SEP event did not extend to very high energies (> 100 MeV), as discussed in the following subsection.
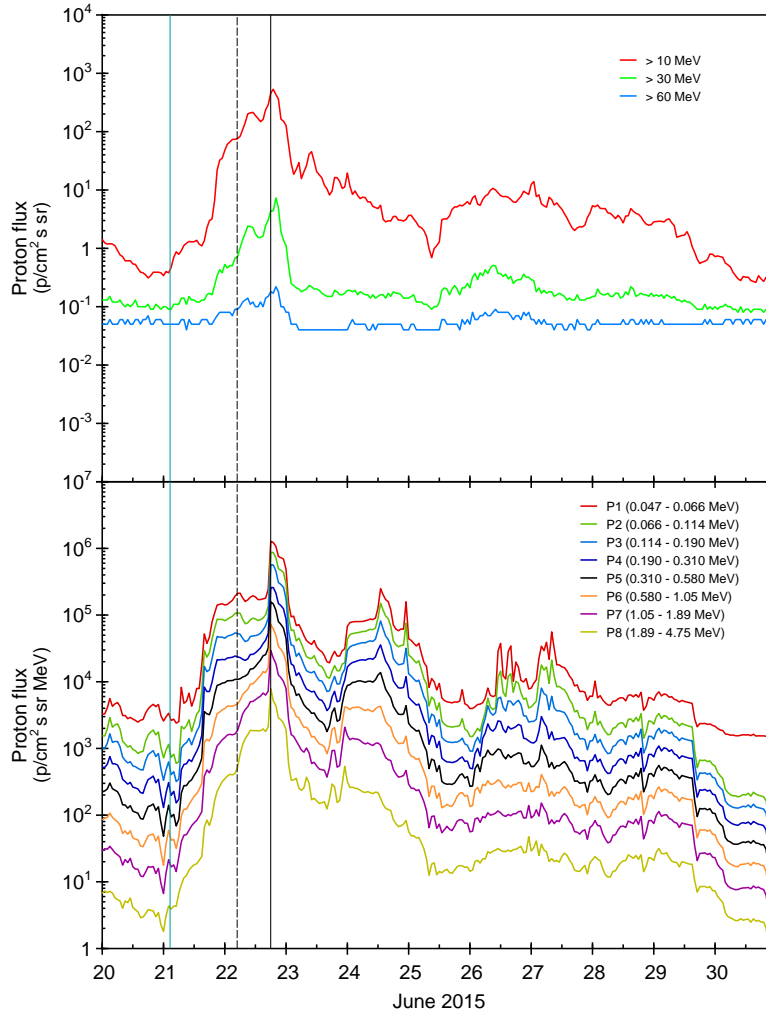
Figure 21. Temporal behavior of the proton integral (top) and differential (bottom) flux as recorded in different energy channels (energy reported in the legend) by EPAD/GOES and EPAM/ACE, respectively, during the 21 June SEP event (http://omniweb.gsfc.nasa.gov). The cyan, dashed black and solid black lines mark the time of the associated flare maximum, 19 June CME-driven shock and 21 June CME-driven shock at ACE, respectively.

The bottom panel of Figure 21 depicts the particle flux recorded by the Low Energy Magnetic Spectrometers instrument of the Electron, Proton and Alpha Monitor (EPAM) onboard the ACE spacecraft in differential energy channels from 0.047 to 4.75 MeV/n. It is apparent that at lower energies, the SEP event almost matches the > 10 MeV time profile.

Another greater than 10 MeV proton event can be distinguished in Figure 21, starting at 03:50 UT on 26 June (in association with an M7/3b flare at 08:16

UT on 25 June from Region 12371), reaching a maximum of 22 pfu (S1-Minor) at 00:30 UT on 27 June and ending 07:55 UT (on 27 June).

### 5.1. HIGH ENERGY OBSERVATIONS - PAMELA apparatus

The PAMELA instrument provide the opportunity to extend the analysis of the SEP event to higher energies. It was launched onboard the Resurs-DK1 Russian satellite by a Soyuz rocket from the Baikonur space centre on the 15th of June 2006 with an inclination of 70° and a nearly circular orbit at an almost stable altitude of ∼570 km. The apparatus core is a permanent magnet with a micro-strip tracker system placed inside the 0.45 T magnetic cavity, used to measure particle deflection with ∼3 μm and ∼11 μm precision in the bending and non-bending views respectively. The ToF system comprises 6 layers of fast plastic scintillators arranged in three segmented planes which provide 12 measurements of the particle velocity, $\beta = \frac{v}{c}$ and ensures albedo (crossing the apparatus from bottom to top) particles rejection. The 16.3 radiation lengths silicon-tungsten electromagnetic sampling calorimeter (mounted below the tracking system) comprises 44 single-sided silicon planes interleaved with 22 plates of tungsten absorbers and its primary use is lepton/hadron separation. A shower tail catcher and a neutron detector, which help to increase hadron/lepton discrimination, lie below the calorimeter. Finally, the tracking system and the upper ToF system are surrounded by a system of 3 anti-coincidence plates made of plastic scintillators which reject secondary particles in the off-line phase of the analysis. More information on the detector can be found in Adriani *et al.* (2014).

For the analysis of the June 2015 21th solar event the PAMELA Real-Time data reduction has been used, together with the standard data selection criteria reported in Adriani *et al.* (2011). We have selected events that do not produce secondary particles in the first two scintillator planes and in the tracker, with a single fitted track within the spectrometer fiducial acceptance. We also required the absence of hits in the anti-coincidences. By using the timing information of the ToF system to evaluate the β of the incoming particle and by requiring β >0, we rejected particles coming from the bottom of the apparatus, which may be part of a population of trapped particles in the geomagnetic field not directly coming from the Sun. To reinforce this condition, constraints on the geomagnetic cutoff are added. Finally, proton selection has been carried out using the information on the energy loss inside the tracker and the Bethe-Bloch formula.

Figure 22 shows the integrated proton flux measured by PAMELA in three energy regions (from 80 MeV to approximately 600 MeV) collected every 4 hours. To allow an easier comparison, we also plot the data from GOES 15 (see http://satdat.ngdc.noaa.gov/sem/goes/). The green vertical line represents represents the maximum time (02:36 UT) of the associated M2.6 flare on the Sun. From the time-profiles of the particles traveling in the heliosphere, some important features can be inferred. The flux profiles show a relatively slow rise to the maximum, as the SEP event originates from a central longitude (W00). Moreover, the profiles shows a little energy extension, falling into background
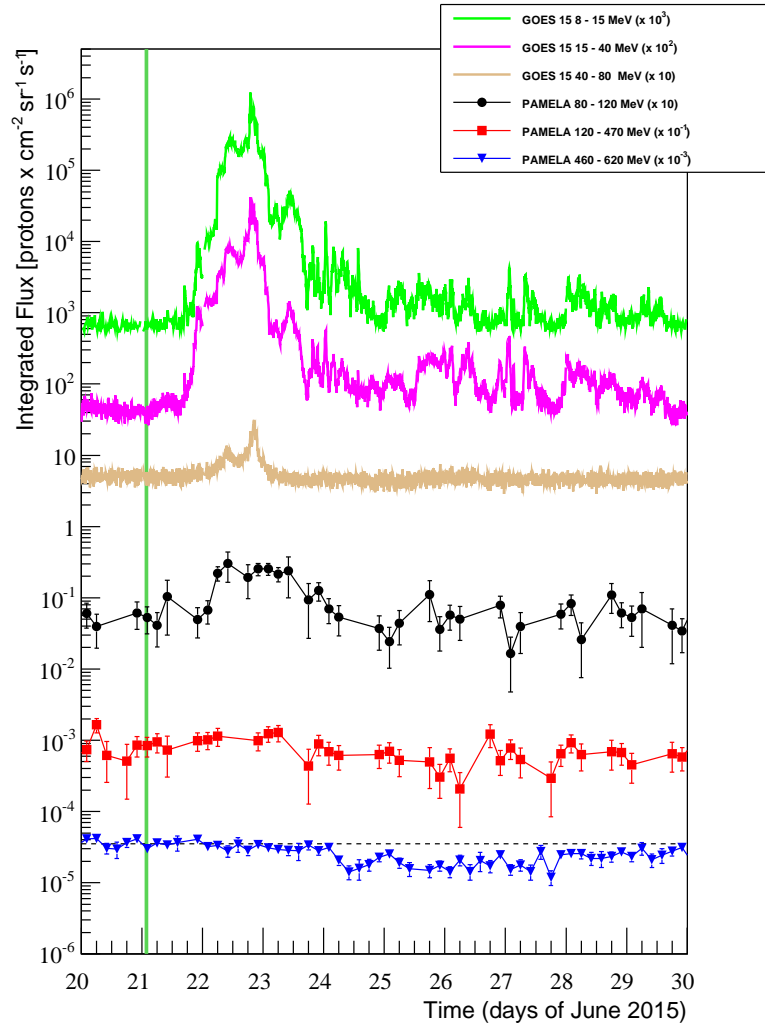
Figure 22. GOES and PAMELA proton fluxes as a function of time in three energy intervals. The vertical green continuous line indicates the onset of the M2.0 flare. The longer data sampling for PAMELA (4 hours) with respect to the GOES one (only 32 seconds) is due to both statistical and orbital limitations. The latter are caused by the magnetic cut-off threshold which blocks the arrival of the low energy particles in specific regions of the Earth. The horizontal black dashed line highlights the undisturbed 460-620 MeV flux and allows comparison with the Forbush flux decrease created by the Halo CME associated to the flare.
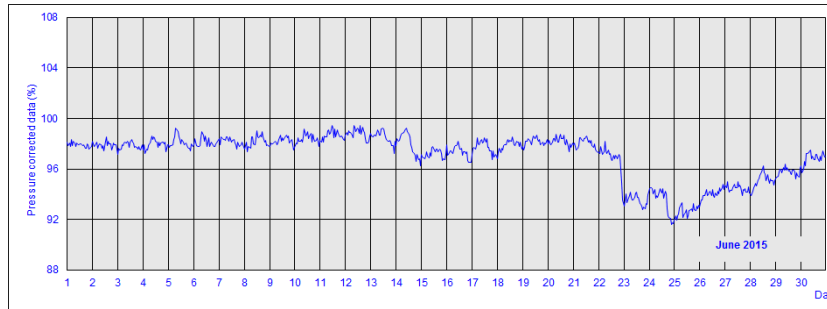
Figure 23. Time history of the cosmic ray intensity recorded at the Rome NM (SVIRCO Observatory) for June 2015.

above ∼120 MeV (red squares) in Figure 22; this means that a small number of particles have been accelerated during the process which is a direct consequence of the fact that the event itself was not powerful enough to accelerate particles beyond this threshold. As stated in the previous section, the two main peaks visible in the GOES observations, are possibly related to two different shocks.

From these data, we can also obtain some more information regarding the CME generated during the event. In fact, the Pamela highest energy fluxes (blue triangles in Fig. 22) suggest the presence of a Forbush decrease after June 23rd (Forbush (1937); Cane (2000)) which is due to the interplanetary counterpart of the full halo CME leaving the solar surface at about 02:30 UT of June 21st.

The Forbush decrease was observed by the worldwide neutron monitor (NM) network. For instance, the Rome NM (geographic coordinates: 41.86°N,12.47°E, sea level; effective vertical cutoff rigidity - Epoch 1995: 6.27 GV) registered about a 5% variation in the cosmic ray intensity, as displayed in Figure 23 (from http://webusers.fis.uniroma3.it/svirco/Dati).

Figure 24 shows the event-integrated differential proton flux as a function of energy measured by PAMELA in the time interval 21st - 24th June (blue circles) with respect to the galactic flux measured in the first 15 days of June (black squares). Both fluxes are scaled to better show the amount of the increase.

5.2. June 21, 2015 SEP event forecasting

The forecast of the June 21, 2015 SEP event is provided by using the model developed by Laurenza *et al.* (2009). The inputs of the model are three solar parameters, i.e., the flare location, the $1 - 8\mathring{A}$ SXR integrated intensity and ~ 1 MHz Type III time-integrated intensity to give a warning for the occurrence a SEP event, within 10 minutes following the flare maximum. The time-integrated SXR intensity is performed between the 1/3 power point before the X-ray peak and the 1/3 power point after it, while, due to the less regularity of the radio emission, the radio time-integration starts 10 minutes before the time of the SXR integration until 10 minutes after the X-ray peak (see Laurenza *et al.* (2009) for more details).
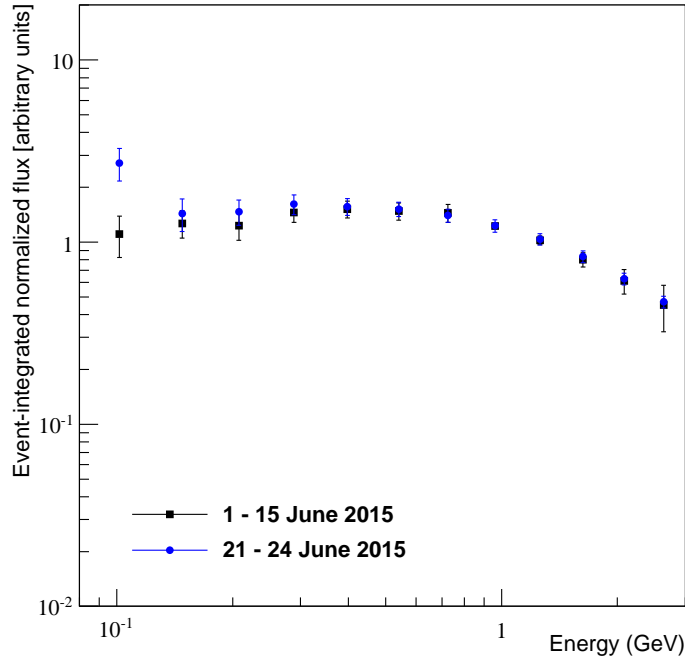
Figure 24. Normalized and event-integrated proton flux (21st - 24th June) as a function of energy, superimposed to the background proton flux (1st - 15th June).

Figure 25 shows the probability contours (solid lines) for SEP forecasting obtained by Laurenza *et al.* (2009) as function of the time-integrated radio intensity at 1 MHz and the time-integrated X-ray flare intensity, for the flare longitude range E40 - W19. The dashed line represents a threshold for the occurrence of a SEP event: if the values of a flare parameters are located above the curve, a SEP event is predicted to occur; if they are under the curve, no SEP event is expected. The values obtained for the M2.6 flare (having longitude W00) associated with the 21 June SEP event are: 0.16 J/m^2 for the SXR fluence and 7.8×10^6 sfu $\times$ min for the $\sim$ 1 MHz Type III time-integrated intensity. It can be seen in Figure 23 that they are higher (see magenta asterisk) than the probability threshold. Hence, a positive forecast is issued at 02:46 UT (10 minutes after the SXR peak) for the 21 June 2015 SEP event, with a leading time of $\sim$ 19 hours before the actual occurrence of the SEP event at 21:35 UT.

6. Magnetospheric Response

The impact of the CME produces several effects on the Magnetosphere-Plasmasphere-Ionosphere system by generating magnetic field variations, destabilization of
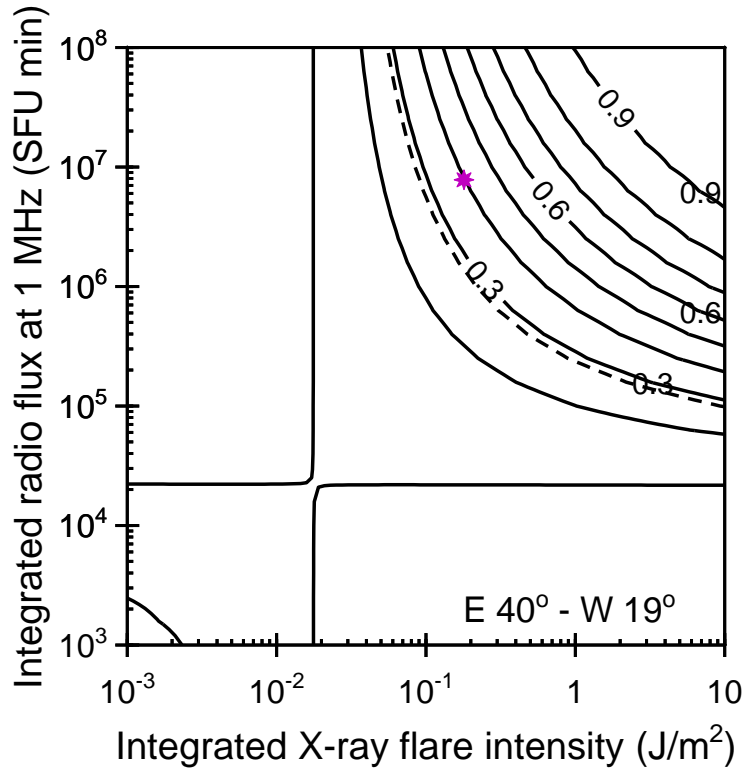
Figure 25. Integrated 1 MHz radio intensity versus integrated 1-8 Å soft X-ray intensity for > M2 soft X-ray flares located in the longitude range E40 - W19: solid lines represent the probability contours; the dashed line is the probability threshold; the magenta asterisk corresponds to the values obtained for the x-ray flare associated with the 21 June SEP event.

magnetospheric and ionospheric current systems, particle injection and precipitation, induced electric fields and large scale ionospheric enhanced plasma convection. This effects can be investigated by using different data sets related to in-situ measurements of fields and particles, through which a comprehensive analysis of the geomagnetic storm can be carried out.

6.1. Geosynchronous analysis

Figure 26 shows the SW and the interplanetary magnetic field (IMF) observations by WIND (box a) and the magnetospheric field observations at geosynchronous orbit (box b) by GOES13 (LT=UT-5) and GOES15 spacecrafts (LT=UT-9). A remarkable interplanetary shock was observed by WIND on 22 June 2015, ∼18:07 UT, at X_{SE} ∼203.0 R_E, Y_{SE} ∼-34.1 R_E, and Z_{SE} ∼-11.0 R_E; it was characterized by remarkable variation of the SW pressure (ΔP_{SW} ∼31.5 nPa) and IMF strength (ΔB_{IMF} ∼22.3 nT), associated with a relevant increase of the southward IMF component ($B_{z,IMF}$ ∼-20.0 nT), persisting for ∼90 min. According to the Rankine-Hugoniot relations, the shock normal was oriented at
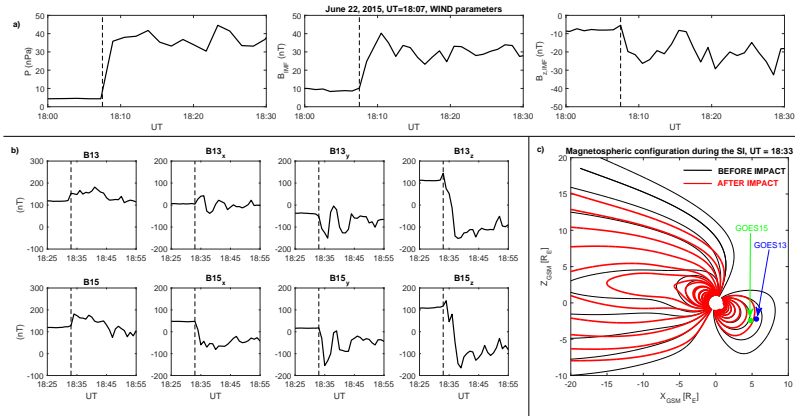
Figure 26. SW parameters as measured by WIND: box a) dynamic pressure, total magnetic field, Z_{SE} component of the IMF. Box b) The magnetic field magnitude and components in the GSM coordinate system as measured by GOES13 and GOES15. Box c) The position of the two geosynchronous satellites and the magnetospheric configuration before (black lines) and after (red lines) the shock impact.

$\Phi_{SE} \sim 186°$, $\Theta_{SE} \sim -9.8°$ and the estimated shock speed was $V_{Sh} \sim 767\,\mathrm{km\,s^{-1}}$. Consequently, the shock impact onto the magnetosphere was predicted at $\sim$18:34 UT ($\sim$27 minutes after WIND observations). In fact, the SI at geosynchronous orbit was observed by both GOES at $\sim$18:33 UT (box b), more clearly in the magnitude of the magnetic field. Interestingly, GOES13 and GOES15 observed a small and rapid enhancement in the Bz ($B13_z$ and $B15_z$) component (associated with the field compression), preceding a sharp transition from $\sim$100 nT to $\sim$-100 nT; at the same time the other components undergo strong variations. According to (Suvorova *et al.*, 2005; Dmitriev *et al.*, 2005), these features are indicative of magnetopause crossing. On the other hand, due the extreme values of the SW parameters, according to Shue *et al.* (1998) model, the magnetopause nose is expected to move inward up to $\sim$4.9 R_E. Figure 26 (box c) shows the predicted configuration of the magnetospheric field lines in the noon/midnight plane before (black lines) and after (red lines) the shock impact (TS05 model, (Tsyganenko and Sitnov, 2005)) and reveals the extreme field compression in the period of interest. Figure 27 (top panel) shows the southward orientation of the B_{IMF} (Bz_{IMF}) between 18:33 - 19:50 UT. Correspondingly, GOES 13 (central panel) and GOES15 (bottom panel) show, in conflict with the northward orientation expected in the wide noon region, a strongly negative orientation at geosynchronous orbit. This feature can be interpreted in terms of a relevant erosion of the magnetopause caused by the strong southward component of B_{IMF} observed in the corresponding interval. In particular, the correlation coefficients between the B_z ($B13_z$ and $B15_z$) component observed by geostationary spacecrafts and Bz_{IMF} are $r_{13} = 0.89$ at GOES 13 and $r_{13} = 0.93$ at GOES15, respectively. On the other hand, in this time interval GOES13 was located between 13:40-15:10 LT and GOES15 between 09:40-11:10 LT, suggesting a way out of both spacecrafts into the transition region.
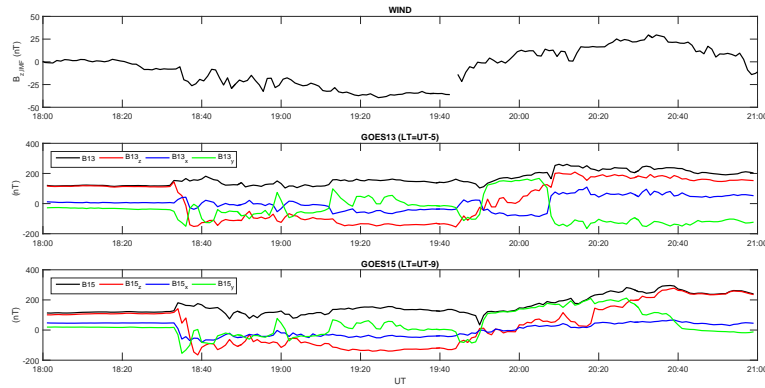
Figure 27. top panel: The Z_{SE} component of the IMF shifted of 27 minutes; central panel: the magnitude of the magnetic field (black line), the X_{SM} component (red line), the Y_{SM} component(blue line) and the Z_{SM} component (green line) in the GSM coordinate system for GOES13; bottom panel: the magnitude of the magnetic field (black line), the X_{SM} component (red line), the Y_{SM} component(blue line) and the Z_{SM} component (green line) in the GSM coordinate system for GOES15. Red shaded regions identifies the period of southward IMF after the shock impact.

6.2. Plasmasphere dynamics

Among the large variety of phenomena produced in the magnetosphere by a geomagnetic storm, a very important one is the significant effect on the cold and dense plasma located in the inner magnetosphere (the plasmasphere). This region, populated by the outflow of ionospheric plasma along low/mid-latitude field lines, approximately co-rotates with the Earth and extends typically up to 4-5 Earth radii (R_E). There is often an abrupt transition (plasmapause) between the dense plasma of the plasmasphere and the more tenue plasma of the plasmatrough which is generally convected toward the dayside magnetopause by a large scale electric field imposed across the magnetosphere by the solar wind-magnetosphere interaction. During a GS the magnetospheric convection intensifies and consequently the plasmasphere is eroded and the plasmapause moves closer to the Earth. The plasma concentration inside the new boundary is also subjected to significant variations, either a decrease or an increase depending on different competitive processes.

These phenomena have been mostly investigated in the past by in situ measurements (Moldwin, 1997) or by whistlers recording on the ground (Carpenter, 1963; Park, 1973). An alternative, more recent, remote sensing technique is based on the detection of geomagnetic field line resonances (FLR) by means of a pair of magnetometer stations slightly separated in latitude (Menk et al., 2014). Cross-phase and amplitude-ratio of the ULF signals recorded at the two stations are used to determine the eigenfrequencies of the field line crossing the midpoint of the stations pair (Baransky et al., 1985; Waters, Menk, and Fraser, 1991). The so determined FLR frequency (usually the fundamental one) is converted to an estimate ρ_{eq} of the cold plasma mass density at the equatorial
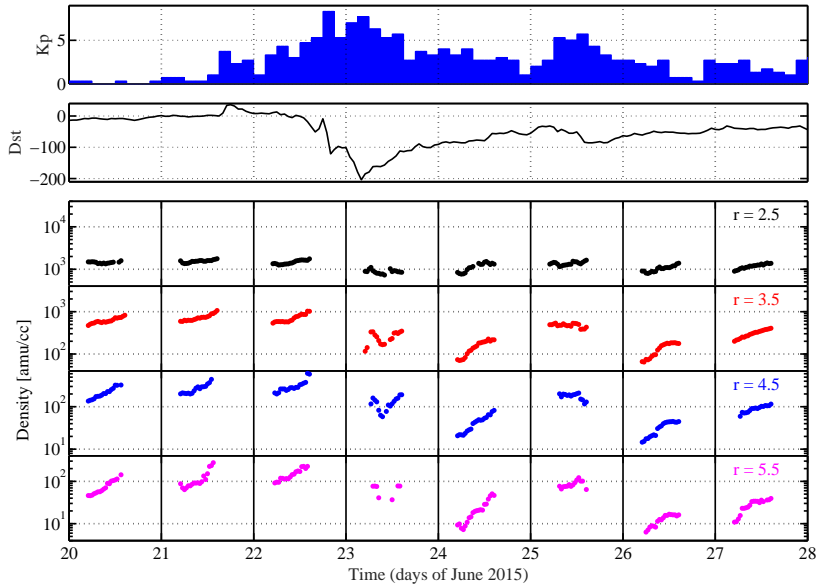
Figure 28. From top to bottom: Kp index, Dst index, FLR-derived equatorial plasma mass densities at different Earth distances over 20-27 June 2015.

point of the field line. This is done by solving MHD wave equations under an appropriate geomagnetic field model and assuming a reasonable profile of the normalized density distribution ρ/ρ_{eq} along the field line (Vellante, Piersanti, and Pietropaolo, 2014).

By means of a latitudinally extended network of stations it is then possible to monitor both temporal and spatial variations of the cold plasma mass density in a considerable portion of the magnetosphere. We used to this purpose the measurements provided by EMMA, a meridional network of 25 magnetometer stations extending from Central Italy to North Finland ($36° < \lambda < 67°$, LT ∼ UT + 2 hr; Lichtenberger *et al.* (2013)). MHD wave equations were solved assuming the T01 Tsyganenko magnetic field model (Tsyganenko, 2002) and the following radial dependence of the field aligned density distribution $\rho/\rho_{eq} = (r/r_{eq})^{-1}$ (Vellante and Förster, 2006). As the equatorial densities derived from a given station pair may refer to a time-changing equatorial distance (especially at high latitudes and for disturbed magnetospheric conditions), ρ_{eq} values were determined at fixed radial distances by interpolating at each time the experimental data points by a smoothing spline curve.

Figure 28 shows the temporal variation of the inferred equatorial plasma mass density at $r = 2.5, 3.5, 4.5, 5.5\ R_E$ over 20-27 June 2015. The data cover only the dayside region (∼07-17 LT) where FLRs are more efficiently excited and the evaluation of the FLR frequency (and the derived density) is more reliable.

Through June 20-22, i.e. before the SSC of June 22 18:36 UT (marked by a distinct peak in Dst), a recurrent daytime pattern of the density is observed at

each r value, characterized by a trend of increasing values through the day which is more pronounced at higher radial distances. Such daytime density increase is caused by the gradual refilling by the ionosphere of the magnetospheric flux tubes which are partially depleted during nighttime hours. Note also a day-to-day increase at 5.5 R_E, indicating that at this radial distance the fluxtubes are still in a phase of recovery following a previous event of high geomagnetic activity.

On June 23, i.e. during the first stage of the storm recovery phase, the general level of the density is significantly decreased by a factor of ∼2 everywhere, but the daily pattern is more confused because of the rapid change in the magnetospheric field configuration and the competitive interplay between the refilling from the ionosphere and the depletion by the enhanced magnetospheric convection.

On June 24, the density at 3.5-5.5 R_E has further decreased (by a factor ∼5-7 with respect to June 22), while at 2.5 R_E has returned to the typical pre-storm level. The significant plasma depletion also gives rise to a more pronounced daytime refilling process at all radial distances.

At the very beginning of June 25 there appears to be an almost complete recovery with respect to the same hours of June 23, but the typical daytime refilling appears to be inhibited by a re-intensification of the geomagnetic activity (see Kp and Dst behavior). The effect of this apparently milder re-intensification of the geomagnetic activity gives rise actually to an even stronger plasma depletion on June 26 with a density decrease of a factor ∼10 at 5.5 R_E. Moreover, the recovery from the plasma depletion event of June 26 is slower than what observed for the depletion event of June 24: the median density on June 27 recovered to ∼ 90% of the pre-storm value at 2.5 R_E, ∼ 45% at 3.5 R_E, ∼ 35% at 4.5 R_E, and only ∼ 20% at 5.5 R_E.

Further information on the temporal-spatial variation of the plasma density is provided by the radial profiles shown in Figures 29 and 30. The profiles in Figure 29 are representative of the radial density variation in the morning side (∼08 LT) while those in Figure 30 correspond to the post-noon region (∼15 LT). A smoothing spline curve (solid line) is drawn through the data points to guide the eye. The dashed line in each panel is the radial profile of June 22 which is drawn as a reference profile representative of the pre-storm condition at the same hour. This reference profile is well fitted by the equation $log_{10}(\rho) = 4.1 - 0.40\ r$ at 06 UT and 4.1 - 0.32 r at 13 UT which are typical of an extended plasmasphere (Carpenter and Anderson, 1992). Note also that the radial profiles for June 23-27 extend to distances greater than the maximum distance (∼6 R_E) covered by the June 22 reference profile. The reason is that the solar wind/magnetospheric conditions for June 23-27 (in particular ring current effects) cause a significant field line stretching modelled by the T01 model (Berube, Moldwin, and Ahn, 2006).

The morning profile shows a dramatic change on June 24 with a steep density falloff starting from ∼2.2 R_E. Such behaviour is indicative of a plasmapause formation between $2 - 3\ R_E$. This is also confirmed by the detection of cross-phase reversals in the FLR analysis between 2.3 R_E and 2.7 R_E which are indicated by circles. This circumstance occurs when the station pair maps an equatorial region where the radial density variation is steeper than r^{-8} as for
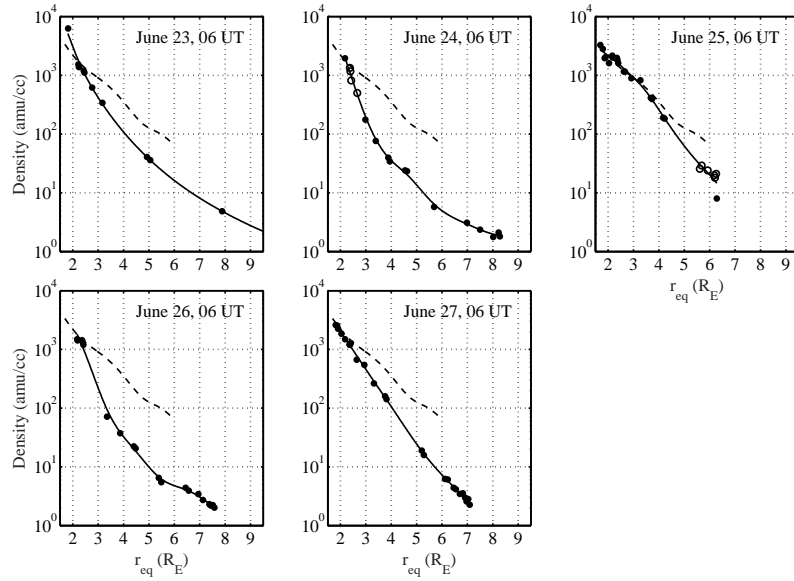
Figure 29. Radial profiles of the inferred equatorial plasma mass density at 06 UT ($\sim$ 08 LT) for 23-27 June 2015. A smoothing spline curve (solid line) is drawn through the data points to guide the eye. The dashed line in each panel is the radial profile of June 22 which is drawn as a reference profile representative of the pre-storm condition at the same hour. Dots are values derived by cross-phase maxima (typical situation) and circles are values derived by cross-phase minima (which are possible indicators of plasmapause).

the plasmapause (Kale *et al.*, 2007). On the next day (June 25) flux tubes up to $\sim$3.5 R_E completely recovered their plasma content while for $r > 3.5$ R_E there is still some level of depletion. There is also a possible evidence of a plasmapause at 5-6 R_E. A new inward displacement of the plasmapause is visible on June 26 at a location ($\sim$2.5 R_E) similar to that of June 24. The results for June 27 confirm that in this case the recovery is slower.

The results for the post-noon region (Figure 30) are similar to those of the morning side except for some evidence of a plasmapause on June 24 and June 26 located at a slightly higher distance. This is in agreement with empirical model predictions by O'Brien and Moldwin (2003).

7. Ground Response

In this Section we will describe the ground effects of the impacts of the solar ejecta on the magnetosphere as measured both to high and low latitude. During the main phase of a geomagnetic storm, several phenomena can be detected by ground stations that reflect into variations of the ionospheric currents and geomagnetic field. In particular, after a brief introduction to the general features of the ground response we investigate the response of the ionospheric current
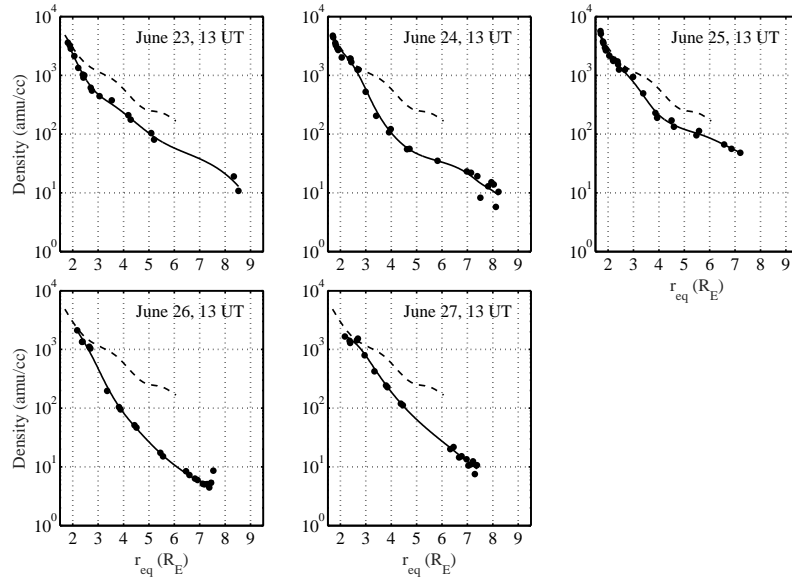
Figure 30. The same as in Figure 2a, but at 13 UT ($\sim$ 15 LT).

to the Storm Sudden Commencement (SSC), the large-timescale contribution of the geomagnetic field detected by ground stations and the high latitude ionospheric convection pattern as detected by the Super Dual Auroral Radar Network (SuperDARN) in the northern polar regions.

7.1. General Features

In Figure 31 we report the high-latitude geomagnetic AE index (Davis and Sugiura, 1966), which is an indirect measure of the energy deposition rate in the polar ionosphere (Ahn, Akasofu, and Kamide, 1983), and the low-latitude geomagnetic SYM_H index, which provides a ground based measurement of the magnetospheric ring current enhancement during magnetic storms. The geomagnetic response is compared to the main changes of the solar wind features at L1 as observed by the ACE spacecraft. Data come from the NSSDC-CDA web data center and refers to 1 min OMNI dataset and ACE magnetic and plasma measurements.

A simple visual inspection of the data reported in Figure 31 shows how the observed high latitude and low latitude geomagnetic response during the investigated time period is highly complex. On June, 22 at 18:37 UT SYM_H shows a large increase (Sudden Impulse - SI) up to 88 nT, which follows the increase of the solar wind flow velocity v and proton density n_p observed by ACE at 17:59 UT. According to Joselyn and Tsurutani (1990) this increase can be considered as the Storm Sudden Commencement (SSC) of the geomagnetic
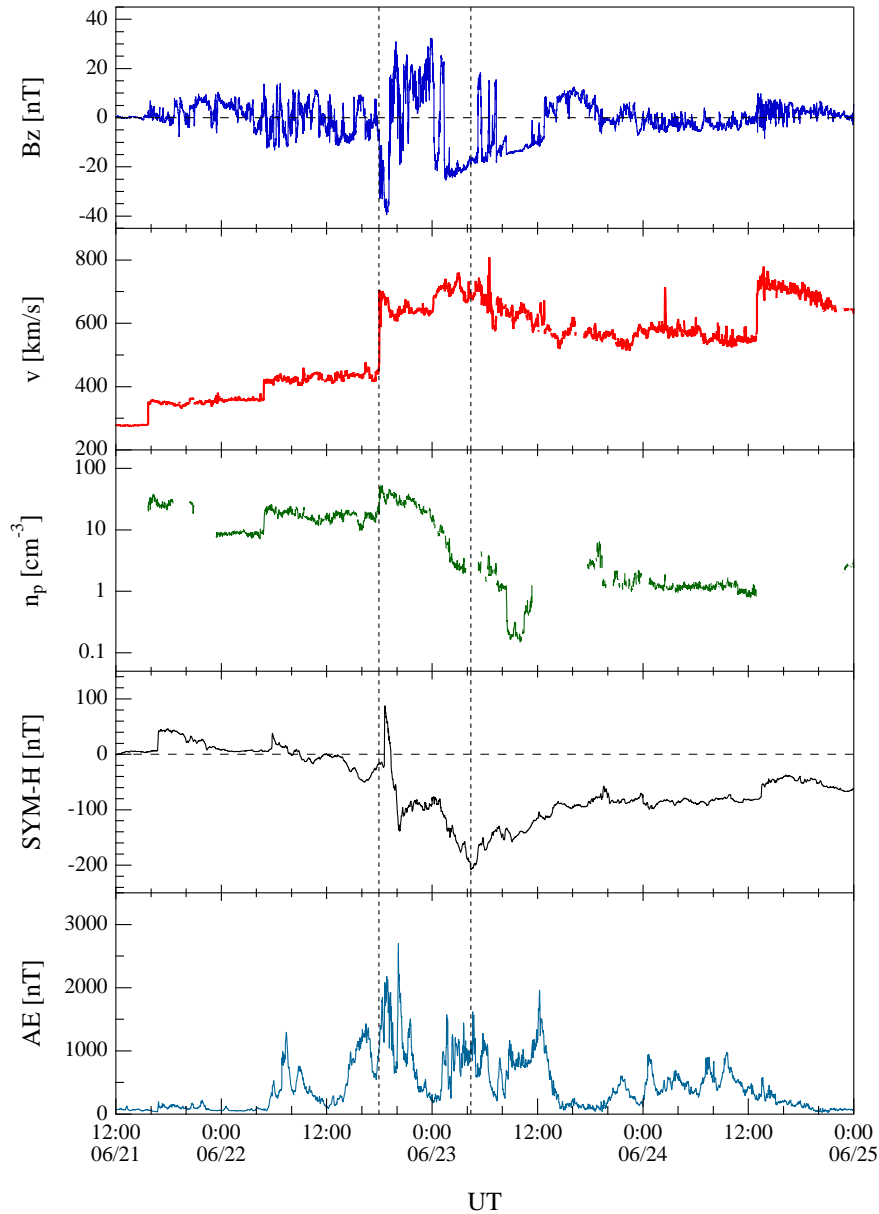
Figure 31. Comparison of the magnetospheric response (AE and SYM_H geomagnetic index) to the solar main interplanetary parameters ($B_{Z,IMF}$ - component of the IMF, v - solar wind flow velocity, n_p - solar wind proton density) as measured at L1 position by ACE spacecraft. The two dashed lines indicates the arrival of IMF CME shock as observed by ACE at 17:59 UT on June,22 and the minimum values reached by SYM_H during the storm main phase on June, 23 at 04:27 UT.

storm occurring on June, 22 and which is the consequence of the solar flares observed on June, 21.

However, we note that, while low-latitude geomagnetic activity mainly follows this SSC, at high latitude the situation is different. Indeed, AE-index shows two distinct periods of small-to-large geomagnetic activity on June, 21 and 22, which precede the large storm of June, 22. These two antecedent periods of activity follow the two SIs observed on June, 21 at 16:47 UT and June, 22 at 05:47 UT (see SYM_H positive increases) and are related to the solar wind flow velocity increases and the rapid southward turnings of the $B_{Z,IMF}$, observed by ACE spacecraft.

Coming back to the June, 22 geomagnetic storm the structure of the storm as revealed by SYM_H index suggests that we are in presence of a double storm. Indeed, after the first rapid decrease of SYM_H value down to -139 nT at 20:17 UT, we observe another large negative peak ($SYM_H = -208$ nT) on June, 23 at 04:27 UT. This double structure resembles the trend of the $B_{Z,IMF}$ component, which shows two periods of nearly stable time intervals of $B_{Z,IMF} < 0$: the first starting at 17:43 UT of June, 22 and the second starting at 01:22 UT of June, 23. As a consequence of these long intervals of negative $B_{Z,IMF}$, the solar wind plasma can flow inside the Earth's magnetosphere due to the possible occurrence of magnetic reconnection at the Earth's magnetopause between the IMF and Earth's magnetic field.

At high latitude the geomagnetic activity is characterized by large bursts of activity as clearly shown by AE-index. This is the evidence of a series of fast relaxation events, perhaps consequence of an activity in the near-Earth's geomagnetic tail regions, which are due to the occurrence of a series of loading-unloading energy releases (Kamide and Kokubun, 1996; Consolini and De Michelis, 2005). The activity of AE-index resembles quite well the changes of SYM_H with time. Indeed, the first AE-index burst is quite well correlated with the SSC, while the other peaks seems to occur in phase with decreases of SYM_H. This is an evidence of what is named storm-substorm relationship. Furthermore, the high latitude geomagnetic activity continues also during the first stage of the storm recovery phase. This successive AE-index activity is very well correlated with the successive negative turnings of the $B_{Z,IMF}$, occurring on June, 23 after the 10:00 UT. However, these successive turnings of $B_{Z,IMF}$ do not affect the recovery phase. This is because they are correlated with a time interval during which the solar wind density decreases to vales below $n_p = 1$ cm^{-3}.

7.2. The SSC characteristics and the ionospheric current flow pattern

Generally, the main phase of a Geomagnetic Storm is preceded by the Storm Sudden Commencements (SSC), caused by the interplanetary fast shocks or discontinuities of the incoming solar wind (SW) colliding with the magnetopause and compressing the magnetosphere. The morphological aspects of SSCs at geosynchronous orbit and in the outer magnetosphere have been studied in several works (Patel and Coleman, 1970; Kokubun, 1983; Lee and Lyons, 2004; Villante and Piersanti, 2008, 2009). At geosynchronous orbit, they show that

the SSC amplitude was remarkably dependent on local time (LT), with highest values at noon and very small values (or even negative, in some cases) in the night sector. On the other hand, at ground the SSC signature shows a more complex behavior, depending upon LT and geomagnetic latitude. The current understanding suggests that the total disturbance field (D_{SI}) can be decomposed into different subfields, namely $D_{SI} = DL + DP$ (Araki). They consist of a step-like structure of magnetospheric origin dominant at low latitudes (DL field, where L stands for *"low latitude"*) and a double pulse structure of ionospheric origin (DP field, where P stands for *"polar latitude"*), dominant at high latitudes; the first and the second pulse are called preliminary impulse (PI) and main impulse (MI), respectively.

Araki developed a model to explain the global behavior of the SI waveform, considering the H component (North-South) alone. According to this model, the SW pressure enhancement increases the magnetopause current that generates a step-like increase, with maximum amplitude at the equator. A two-cell ionospheric currents (DP 2-type currents), induced by a dusk-to-dawn electric field along the compressional wave front, produce a preliminary impulse of polar origin (PI). On the other hand, if the SW dynamic pressure persists high, the magnetospheric convection adjusts itself to the compressed state determining a new ionospheric vortex system (opposite to the PI), corresponding to the main impulse (MI). It is driven by the electric field that originates in the polar region and is transmitted from the outer magnetosphere through field aligned currents (FAC), which flow into the ionosphere in the morning side and away in the afternoon side. The amplitude and waveform of the magnetic field variation strongly depend on latitude and LT (Araki; Piersanti and Villante, 2016). At low latitudes, the DP field is characterized by a positive variation along the H component, whose amplitude maximizes around local noon, and by a negligible/null variation along the D component. Araki T. and T. (2009) showed that both PI and MI fields are produced by a combination of FACs and ionospheric currents, so that:

$$\begin{aligned} DP &= PI + MI \\ PI &= PI_{FAC} + PI_{IC} \\ MI &= MI_{FAC} + MI_{IC} \end{aligned}$$

Recently, Piersanti and Villante (2016) developed a technique to discriminate between the DL and the DP fields from ground SI observations, inferring the double ionospheric current vortices for both the PI and the MI. They estimated the DL field by comparing the magnetospheric field observations and Tsyganenko and Sitnov (2005) model previsions. The DP field is obtained by subtracting the estimated DL field from ground observations.

Here, we applied the Piersanti and Villante (2016) technique to 63 ground magnetic observatories in the northern hemisphere to derive ionospheric current flow pattern associated to the June 22, 2015 SSC. For this purpose, we used the INTERMAGNET (International Real-time Magnetic Observatory Network - http://www.intermagnet.org/index-eng.php) global network of observatories for

ground measurements and the Van Allen probes data for magnetospheric observations. On the basis of Piersanti and Villante (2016) scheme, we compared both RBSP-A and RBSP-B magnetospheric field data with the $TS04$ (Tsyganenko and Sitnov, 2005) predictions for different magnetospheric current configurations (not shown), obtaining that the sum of the Chapman-Ferraro current and the Tail current (B_{CF+T}) provides the best representation of the magnetospheric response to the SI disturbance. This result, at ground, allows to estimate the DL field by means of the B_{CF+T} field along both the H and the D component. The residual DP fields is determined subtracting the estimated DL_H and DL_D fields from ground magnetic observations. Figure 32 shows typical examples, in which the black traces represent the experimental observations and the red dotted lines the DL_H and DL_D fields (top panels). In each box, the bottom panels show the estimated DP fields. As a matter of facts, similar characteristics of the ground response emerge in definite latitudinal (λ, being the corrected geomagnetic latitude) and local time (LT) sectors:

- **Low latitude** ($\lambda<30°$; Box a): the response (upper panels) is characterized by a stepwise variation of the H component and a small negative variation of the D component. The DP field (bottom panels) shows a negative (PI) then positive variation (MI) along H and opposite smaller signatures along D.

- **Mid latitude** ($30°<\lambda<50°$; Box b): the H component shows a huge increase well above the expected level followed by a sharp decrease to the predicted level, while the D component shows a negligible/null variation in the afternoon region ($13<LT<20$, not shown), a small negative then positive variation in the morning sector ($08<LT<12$, not shown) and a negligible/null variation in the nightside region ($21<LT<06$). The DP field shows different characteristics depending on LT. In the afternoon sector (not shown) it shows a negative PI that is followed by a positive MI along the H component and a negligible/null variation along the D component. In the morning sector (not shown), a positive PI is followed by a negative MI along H and a small negative PI is followed by a small positive MI along D. In the nightside region, (bottom panels), a negative PI precedes a huge positive MI along the H component and a smaller negative PI and positive MI along the D component.

- **High latitude** ($50°<\lambda<80°$): in the morning sector ($8<LT<11$, Box d, upper panels) superimposed to the step-like variation, the response is characterized by a huge and rapid positive then negative variation along H and by a much smaller negative then positive variation along D; in the afternoon sector ($13<LT<20$, not shown), the long term variations are almost null; the H component shows a sharp negative then positive variation, while the D component shows a smaller positive then negative variation; in the nightside sector ($21<LT<06$; Box d, upper panels) the H component shows a huge increase well above the expected level followed by a sharp decrease to the predicted level, while the D component shows a negligible/null variation. The DP field signature strongly depends on LT. In the morning (Box d, bottom panels) a negative PI is followed by a positive MI along H, with
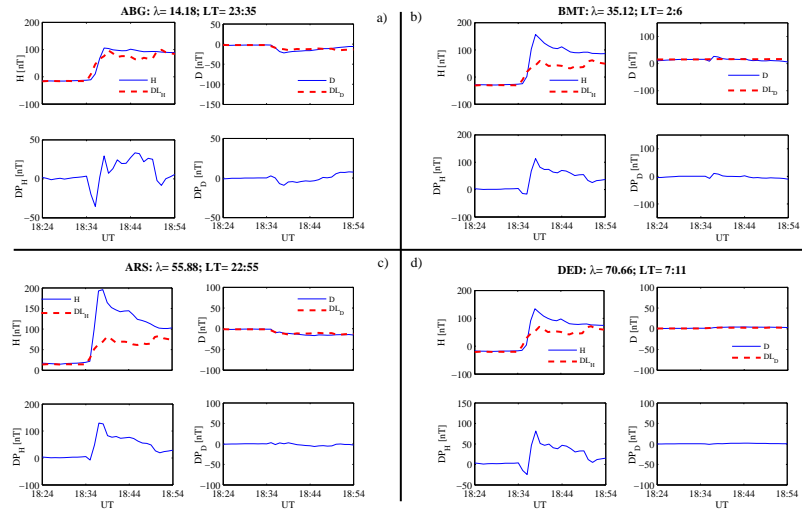
Figure 32. Box a) equatorial latitude SSC example (ABG: λ =14.18°; LT=23:35); Box b): mid latitude SSC example (BMT: λ =35.12°; LT=02:06); Box c): high latitude night SSC example (ARS: λ =55.88°; LT=22:55); Box d): high latitude morning SSC example (ABK: λ =70.66°; LT=07:11). In each box: top panels show the H (left) and the D (right) traces superimposed to the estimated DL_H and DL_D fields, respectively (red dashed line); bottom panels show the residual DP fields for both H and D components.

negligible/null variation along D; in the afternoon sector (not shown), a positive PI is followed by a negative MI along H and a positive PI is followed by a negative MI along D; in the nightside sector, a positive MI follows a negative PI along H with negligible/null variation along D.

On the basis of the results obtained for the DP fields, we evaluated the ionospheric origin fields (PI_{IC} and MI_{IC}) at each ground station. The global results for PI_{IC} and MI_{IC} vectors, as obtained at 63 ground stations, are summarized in Figure 33, which shows the direction of the ionospheric current for the PI_{IC} (panel a) and the MI_{IC} (panel b). The behaviour is consistent with a morning counter-clockwise (CCW) and an afternoon clockwise vortices (CW) for the PI_{IC} and a morning CW and an afternoon CCW vortices for the MI_{IC}, respectively. The vortices focuses results to be approximately located at $\lambda \sim 58°$ and $LT \sim$06:30 and at $\lambda \sim 58°$ and $LT \sim$17:00. Lower latitude stations show almost horizontal directions (West-East for the PI_{IC} and East-West MI_{IC}) as expected for the equatorial SI ionospheric circulation. These results are in agreement with Araki and with Piersanti and Villante (2016). Panels c and d show the amplitude of the PI_{IC} and MI_{IC} fields vs latitude in the dayside sector (06<LT<18). In agreement with Piersanti and Villante (2016), both PI_{IC} and MI_{IC} field amplitudes increase with latitude and the experimental points can be approximated by an exponential function (black dashed lines), such as: $PI_{IC}(\lambda) = PI_0 \cdot e^{A \cdot \lambda}$, $MI_{IC}(\lambda) = MI_0 \cdot e^{B \cdot \lambda}$, with $PI_0 = 2.19$ nT, A =0.06°$^{-1}$ and $MI_0 = 5.25$nT, B=0.10°$^{-1}$. Here, PI_0 and MI_0 are the PI_{IC} and MI_{IC} amplitude inferred at the equator ($\lambda = 0°$). The outliers at lower latitudes might
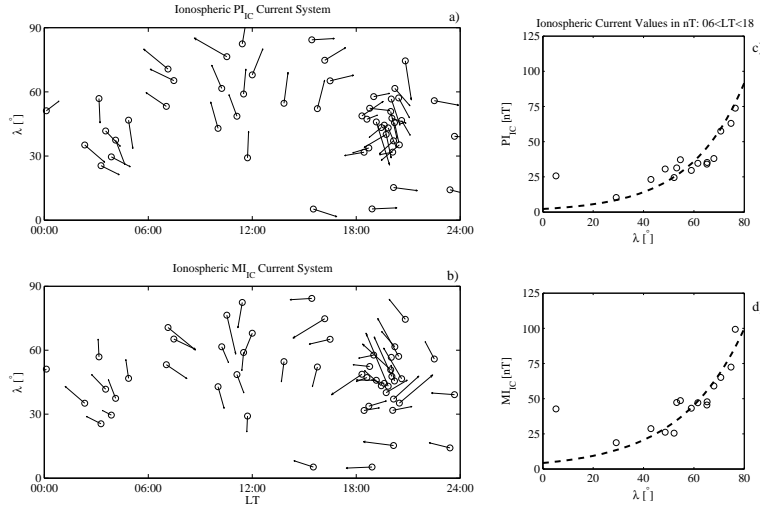
Figure 33. Panels a) and b): the direction of the ionospheric currents for the PI_{IC} (a) and for the MI_{IC} (b), as a function of latitude and local time after a 90° rotation of the disturbance magnetic field. Panels c) and d): the characteristics of the PI_{IC} (c) and MI_{IC} (d) amplitude fields as a function of latitude in the dayside sector (06<LT<18); dashed lines represent the exponential fits and black circles represent the morning PI_{IC} and MI_{IC}.

Table 3. List of geomagnetic observatories.

| Station name	IAGA code	Geographic latitude (λ_g)	Geographic longitude (ϕ_g)
Lviv	LVV	49.90 N	23.75 E
Belsk	BEL	51.83 N	20.80 E
Niemegk	NGK	52.07 N	12.68 E
Hel	HLP	54.60 N	18.82 E
Uppsala	UPS	59.90 N	17.35 E
Lycksele	LYC	64.06 N	18.07 E
Abisko	ABK	68.36 N	18.82 E
Resolute Bay	RES	74.70 N	26.10 E

be related to the equatorial electrojet and could be used as an estimate of its strength.

7.3. Baseline Response

For our analysis, we used 1 minute data from the horizontal component of the geomagnetic field (H) measured at permanent geomagnetic observatories distributed in the Northern hemisphere from mid-latitude to high-latitude, obtained from INTERMAGNET as shown in figure 34.

The data were collected from 8 permanent geomagnetic observatories as reported in Table 3 during the period 15-30 June, 2015. To study the large-timescale variations of the geomagnetic field during the occurrence of a geo-
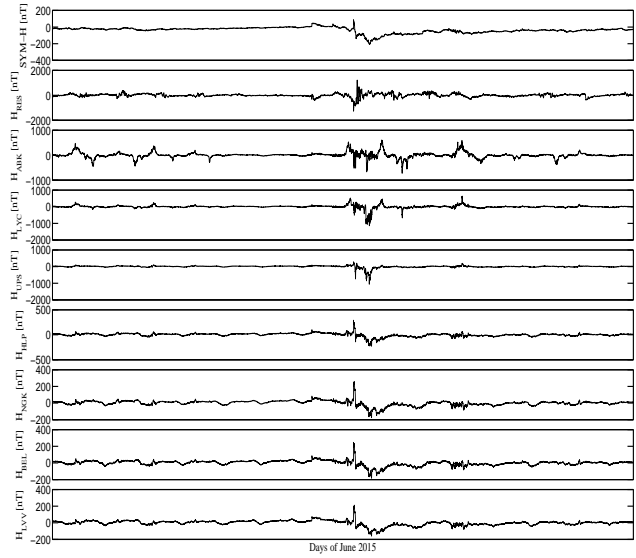
Figure 34. From top to bottom: Sym-H index and H component measured at geomagnetic observatory (with decreasing latitude).
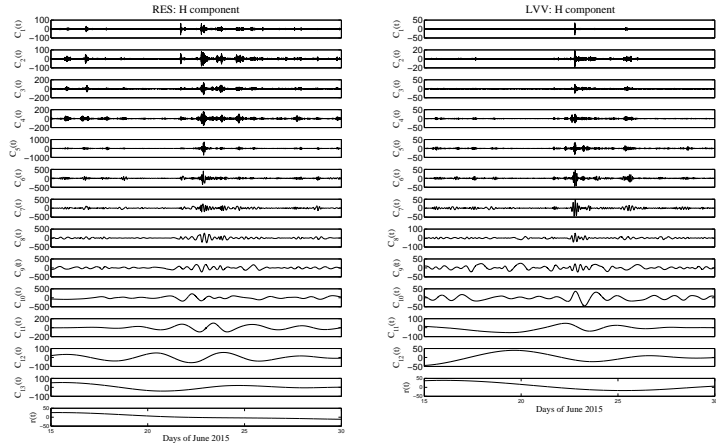
Figure 35. EMD results from the H component measured at RES [left panels] and LVV [right panels] geomagnetic stations, respectively.

magnetic storm, we use the Empirical Mode Decomposition technique (Huang *et al.*, 1998) (see Appendix A for more details). An example of EMD results is reported in figure 35 where the decomposition is applied to the high-latitude RES time series and to the low-latitude LVV record, respectively.

In this way, we extract the intrinsic timescale components of each time series, ranging from few minutes to days. Typically, processes on short-timescale ($\leq$ 24 hours) are involved in the magnetosphere-ionosphere coupling and produce

effects on the ground, through the current systems flowing in the ionospheric region and in the Earth's upper mantle (Feldstein and Zaitzev, 1968; Dominici P., 1997; De Michelis, Tozzi, and Consolini, 2010). Conversely, large-timescale processes ($>$ 24 hours) are related to the direct contribution of the geomagnetic field variations which we identified as the baseline component of the time series. For these reasons, we divided each set of modes into two different subsets: the short-timescale component, which involves empirical modes with a characteristic timescale lower than 24 hours, and a large-timescale components (named H_0), characterized by intrinsic oscillations on timescales greater than 24 hours. Here, we are particularly interested in the study of the large-timescale components because it can be used as a measure of the geomagnetic response to solar wind changes, related to the Ring current and equatorial electrojet activities. Indeed, several low-latitude geomagnetic indices (i.e. SYM_H, Asy_H, Dst) have been proposed to monitor changes in the equatorial current systems (e.g. ring current and equatorial electrojet). Particularly, the SYM_H index is determined by the geomagnetic H component derived from 6 near-equatorial ground magnetometer, unevenly distributed in longitude and latitude, far from the auroral oval region to eliminate the effects of the ionospheric auroral electrojets (Gonzalez et $al.$, 1994; Wanliss and Showalter, 2006). It is calculated by removing the geomagnetic main field and the quiet solar daily variation from the observed magnetometer data, by transforming it into a dipole coordinate system and finally by evaluating the weighted average over the 6 stations of the deviation of the H component from a quiet day (with a weighting factor that is the reciprocal of the cosine of the magnetic latitude of each station). In this way, it represents the average disturbance of the H component that is thought to be symmetric about the Earth, generally attributed to the symmetric ring current activity. For these reasons, since the large-timescale component extracted via the EMD procedure does not contain any oscillation with a characteristic timescale lower than 1 day (for example, a signature of the ionospheric solar quiet variation), it is similar to the Sym-H index but it can be evaluated for each station (not only for equatorial stations) and can be used as a local measure of the time-dependent geomagnetic average field.

Figure 36 shows the time-latitude behavior of the baselines H_0 obtained from EMD reconstructions and the time-behavior of the SYM_H index.

As shown in figure 36, for each day, the intensity of the baseline increases with latitude, indicating that large-amplitude fluctuations are more pronounced in the auroral region, particularly evident during the geomagnetic storm (22-23 June 2015). This suggests that the large-timescale field, which is free by short-timescale contributions related to the internal dynamics of the magnetosphere and to the ionospheric effects, follows the solar wind driver (CME) that impacts the magnetosphere. Indeed, by a comparison with the SYM_H index, we note that the time-behavior of the baseline is similar to the SYM_H index time-evolution, but with different polarity patterns, according to the different latitude considered. Particularly, in the high-latitude region (from geomagnetic latitudes $\geq 70°$), the baseline behavior is different from the mid-latitude one. While mid-latitude baselines follows the time-behavior of the SYM_H index, with a time shift when latitude decreases (as a consequence of the effects of the perturbation
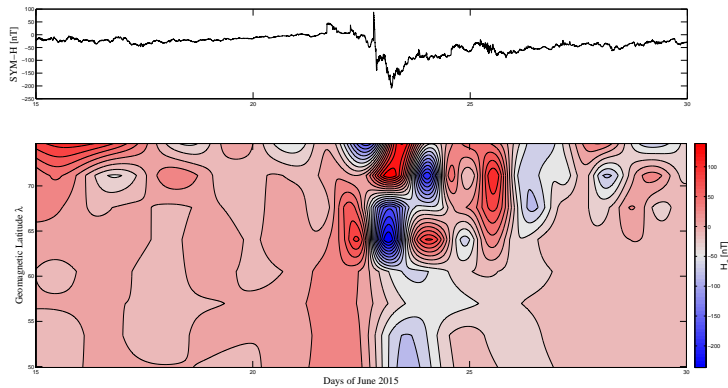
Figure 36. [upper panel] Time behavior of the Sym_H index during the time period under investigation. [lower panel] Time-latitude behavior of the baseline extracted via the EMD procedure from each geomagnetic stations.

at different latitudes), high-latitude baselines presents an opposite time-behavior with respect to the SYM_H index. This could be related to the different current systems encountered by the perturbation when it propagates from high to mid latitudes.

7.4. Ionospheric Polar Convection

In this sub-section we present the observations of the ionospheric convection pattern as observed by the Super Dual Auroral Radar Network (SuperDARN) in the northern polar ionosphere. This network consists of more than 30 high-frequency (8-20 MHz) coherent scatter radars, that via the Doppler shift between the emitted signal and the reflected one provide an estimation of the velocity of the ionospheric plasma convection over the polar regions. Furthermore, Super-DARN is also able to provide information on the features of the decameter-scale plasma irregularities in the E and F regions of the ionosphere (Chisham *et al.*, 2007).

To reconstruct the 2D ionospheric plasma flow we make use of the representation developed by Ruohoniemi and Baker (1998) in terms of "potential maps". This representation combines the measurements from all the available SuperDARN radars with data from the statistical model by Ruohoniemi and Greenwald (1996) to yield a convection pattern covering the entire convection zone.

Figure 37 shows the increase of the ionospheric polar convection observed in the northern ionosphere during the occurrence of the SSC. The SuperDARN radars back scatter echoes are very few before the SSC but the measured velocity vectors are consistent with the two cell convection pattern expected for a predominately negative $B_{y,IMF}$, although the convection around 12 MLT is probably mainly determined by the statically model. At the time of the SSC and in the following period, the two symmetric cells with the antisunward flow
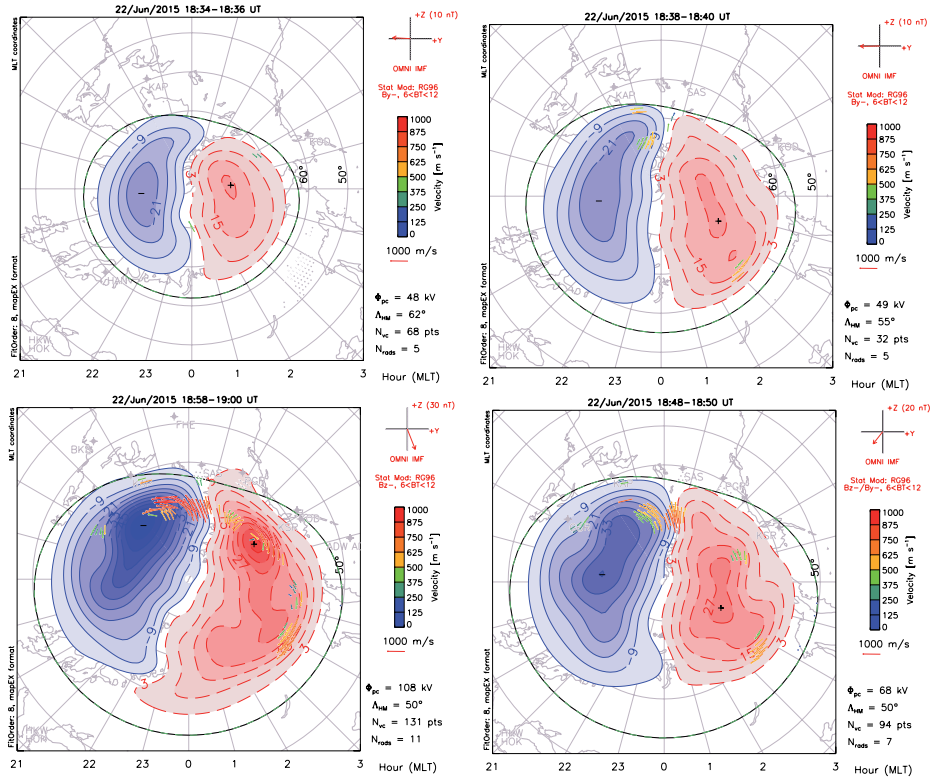
Figure 37. Evolution of the northern ionospheric polar convection pattern during the SSC of June, 22 from 18:34 UT to 19:00 UT. Images are disposed in a clockwise sequence starting from the one on top-left.

in the polar cap, which are characteristic of the predominately negative $B_{z,IMF}$ convection pattern, show a large increase. In particular, the lower boundary of the convection region (the Heppner-Maynard boundary - the black-green dashed circle in the polar maps) shows an expansion towards low latitudes (from 60° N to 50° N). This boundary follows the expansion of the auroral oval in that regions. The increase of the ionospheric polar convection is also clearly demonstrated by the increase of the cross polar cap potential Φ_{pc} up to the very high value of 108 kV near the saturation limit (Shepherd, Greenwald, and Ruohoniemi, 2002).

Figure 38 shows the ionospheric convection pattern in proximity of the maximum level of geomagnetic disturbance ($SYM_H \sim -200$ nT) occurring June, 23 at 04:27 UT. The SuperDARN radars back scatter echoes are present only in the night side around 24 MLT. The two convection-cells reaches low latitudes ($\sim 50°$ N) in the midnight sector indicating a large expansion down to these latitudes of the auroral oval as also shown by the profile of the Heppner-Maynard boundary.

During the recovery phase the two cell convection structure shrinks (see e.g. Figure 39) and all the auroral oval contracts to high latitude regions ($\lambda_g > 60°$ N). This implies also a strong reduction of the polar cap potential toward small
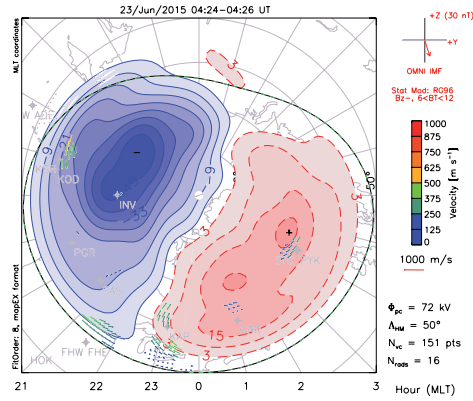
Figure 38. The ionospheric polar convection pattern near the minimum of SYM_H on June, 23 at 04:25 UT as reconstructed from SuperDARN. The solid black curve is the Heppner-Maynard boundary.
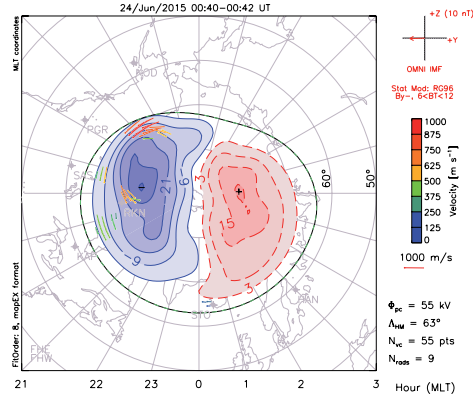
Figure 39. The ionospheric polar convection pattern at the end of the recovery phase on June, 25 at 00:03 UT. The solid black curve is the Heppner-Maynard boundary.

values (few kV). These effects are very well visible in Figure 39 which shows a characteristic situation during the late recovery phase.

8. Summary and Conclusions

The solar trigger of the halo CME is a violent energy release that occurs in the δ complex of AR NOAA 12371. Two subsequent M2.0 and M2.6 flares take place in this region. The X-ray emission shows no interruption, so that these flares can be considered a unique event. The plasma dynamics along the PIL exhibit long-lasting upflows and downflows, suggesting shear accumulation in this location. The flares involve a large area, as shown in EUV images. The events evolve through the destabilization of several coronal structures, in a manner reminiscent of a domino effect. The analysis of the shear angle, of the gradient of the vertical magnetic field and of the electric current indicates that an energy

storage mechanism, compatible with shear accumulation, is active before the eruption. After the flares, the region of the δ complex achieves a more relaxed state.

The availability of a polarized sequence acquired exactly at the right moment during the transit of the halo CME front in the LASCO-C2 field-of-view allowed us to perform a 3D reconstruction of the eruption with polarization ratio technique. Results show that the plasma is expending almost homogeneously at all latitudes, but with a prominent inclination with respect to the plane of the sky around 25°. This allowed us to derive a deprojected CME front speed which, due to CME deceleration, is quite small at large distances (330 km s^{-1} at $\simeq 27.6 R_{sun}$). The application of a simple 1D drag-based model for the interplanetary CME propagation led us to conclude that the early arrival time observed by ACE at 1 AU can be reproduced only by assuming an average propagation speed of about 1440 km s^{-1}, much larger than the deprojected CME front speed.

A SEP event was observed on 21 June 2015, which can be associated with the M2.6 flare (peak time on June 21 at 02:36 UT) occurring in the active region 12371, located at N13W00, and the concomitant full halo CME at 02:36 UT. This SEP event was also accompanied by Type II and Type IV radio sweeps, indicating the presence of a propagating interplanetary shock, and Type III radio signatures. The observed, associated proton fluxes at all of the energy channels show a gradual rise in the prompt phase (as expected for a central meridian event) and a maximum value. By using the model developed by Laurenza *et al.* (2009), we we able to forecast the SEP event at 02.46 UT (10 minutes after the SXR peak) for the 21 June 2015 event, with a leading time of ~ 19 hours before its observed occurrence.

A remarkable interplanetary shock, characterized by extreme values of the SW dynamic pressure and of the southward component of the IMF, was observed by ACE at 17:59 UT and by WIND at 18:07 UT, on June 22, 2015. The time delay between the two spacecraft, estimated using the shock speed V_{Sh} (~ 767 km s^{-1}), obtained applying the Rankine-Hugoniot relations (~ 7 min), is in agreement with the observations (~ 8 min). The magnetospheric response to the shock arrival (18:33 UT)is characterized by a relevant erosion of the magnetopause caused by the strong southward component of B_{IMF} observed in the corresponding interval.

The plasmasphere dynamics shows a first significant erosion up to ~ 2.5 R_E on June 24. Most of the plasma loss was presumably due to a strong electric field convection toward the dayside magnetopause during June 23. An almost complete recovery (at least up to ~ 4 R_E) was observed on the morning of the next day (June 25). A similar (or even stronger) plasmasphere depletion (density decrease of a factor ~ 10 at 5.5 R_E) was observed on June 26 in correspondence to a new magnetospheric disturbance occurring on June 25. In this case the subsequent plasmasphere recovery appeared to be much slower than in the first case and more in line with previous observations (Park, 1974; Chi *et al.*, 2000). The results demonstrate that the FLR-technique is indeed a very powerful method for monitoring the dynamics of the plasmasphere. However, the typical lack of FLR signatures during nighttime does not allow to completely follow all phases

of the geomagnetic storm. A larger, longitudinally extended, network would be necessary to get a more complete picture of the plasmaspheric dynamics during such events.

On June, 22 at 18:37 UT SYM_H shows a large SSC (up to 88 nT) that precedes the geomagnetic storm occurring on June, 22, due to the June, 21 solar flares. The SSC is characterized by a double pulse structure (PI_{IC} and MI_{IC}) whose amplitude and wave forms depends on the latitude and local time of the observatories. Both PI_{IC} and MI_{IC} produced a twin ionospheric current vortices that completely modified the quiet ionospheric current pattern. We found that the behaviour of the ionospheric current associated to the June 22 SSC is consistent with a morning counter-clockwise (CCW) and an afternoon clockwise vortices (CW) for the PI_{IC} and a morning CW and an afternoon CCW vortices for the MI_{IC}, respectively. The vortices focuses results to be approximately located at $\lambda \sim 58°$ and $LT \sim 06:30$ and at $\lambda \sim 58°$ and $LT \sim 17:00$. Lower latitude stations show almost horizontal directions (West-East for the PI_{IC} and East-West MI_{IC}) as expected for the equatorial SI ionospheric circulation. These results are in agreement with Araki and with Piersanti and Villante (2016). Moreover, the ionospheric convection pattern, as observed by SuperDARN in the northern polar ionosphere, is characterized by the well known two cells structure, with the antisunward flow in the polar cap (typical of the predominately negative $B_{z,IMF}$), which during and after the SSC shows a large increase. In particular, the lower boundary of the convection region (the Heppner-Maynard boundary - the black-green dashed circle in the polar maps) shows an expansion towards low latitudes (from $\lambda_g = 60°$ N to $\lambda_g = 50°$ N), especially in the midnight sector. This boundary follows the expansion of the auroral oval in that regions. The increase of the ionospheric polar convection is also clearly demonstrated by the increase of the polar cap potential Φ_{pc} up to 108 kV.

In addition, applying the Empirical Mode Decomposition technique (Huang *et al.*, 1998) on data collected from 8 permanent geomagnetic observatories, we studied the large-timescale variations of the geomagnetic field during the occurrence of the geomagnetic storm. We identified two characteristic timescale ranges of variability:

i) processes on short-timescale (≤ 24 hours) that are involved in the magnetosphere-ionosphere coupling, producing ground effects through the current systems flowing in the ionospheric region and in the Earth's upper mantle (Feldstein and Zaitzev, 1968; Dominici P., 1997; De Michelis, Tozzi, and Consolini, 2010)

ii) large-timescale processes (baseline, > 24 hours) which we related to the direct contribution of the geomagnetic field variations (baseline component).

We found that the baseline increases with latitude, suggesting that the large-timescale field, which is free by short-timescale contributions related to the internal dynamics of the magnetosphere and to the ionospheric effects, follows the solar wind driver (CME) that impacts the magnetosphere. Moreover, by a comparison between the SYM_H index and the baselines, we note that their time-behavior are similar, but with different polarity patterns, according to the different latitude considered.

Interestingly, observations of the ionospheric convection pattern from Super-DARN in the northern polar ionosphere during the maximum level of geomagnetic disturbance ($SYM_H \sim -200$ nT) shows two convection-cells, that reaches low latitudes ($\sim 50°$ N) in the midnight sector, indicating a large expansion down to these latitudes of the auroral oval as also shown by the profile of the Heppner-Maynard boundary. On the other hand the same observations, made during the recovery phase, of the geomagnetic storm, shows a shrink of the two cells convection structure and a contraction of all the auroral oval to higher latitudes ($\lambda_g > 65°$ N). This implies also a strong reduction of the polar cap potential toward small values (few kV).

Appendix

A. Empirical Mode Decomposition

The Empirical Mode Decomposition (EMD) is a useful data analysis technique to investigate non-stationary time series (Huang *et al.*, 1998). It is based on the so-called *sifting* process that allows to extract intrinsic oscillatory components, named intrinsic Mode Functions (IMFs), without any *a priori* assumption on the basis functions, which are directly derived from the data (Huang *et al.*, 1998), via an iterative procedure. The number of sifting steps to obtain an IMF is defined by the stopping criterion proposed by Huang *et al.* (1998), based on the standard deviation between two iteration steps, which must be smaller that a threshold value, typically fixed between 0.2 and 0.3 (Huang *et al.*, 1998). In this way, a discrete time series $S(t)$ can be decomposed into a set of finite number N of IMFs and a residue $r(t)$ (which is not an IMF) so that

$$S(t) = \sum_{i=1}^{N} C_i(t) + r(t) \tag{2}$$

Each empirical mode $C_i(t)$ satisfies two properties: (i) the number of extrema and the number of zero-crossings must either be equal or differ at most by one; (ii) at any point (locally), the mean value of the envelope defined by the local maxima and by the local minima is zero. Moreover, by using the so-called Hilbert-Huang transform (Huang *et al.*, 1998), each IMF $C_i(t)$ can be written as a local oscillatory function which presents amplitude and phase modulation, as $C_i(t) = A_i(t) \cos[\phi_i(t)]$, where $\phi_i(t)$ is named instantaneous phase of the i-th mode (see Huang *et al.* (1998) for more details). Consequently, from the time-derivative of the instantaneous phase it is possible to obtain the instantaneous frequency $\omega_i(t) = d\phi_i(t)/dt$, which, different from Fourier or Wavelet analysis, is time-dependent. In addition, a characteristic timescale oscillation can be estimated for each IMF as $T_j i = 2\pi/ < \omega_i(t) >_t$ ($<>_t$ represents the time average).

The EMD has been applied in many different fields, from solar physics (Terradas, Oliver, and Ballester, 2004; Vecchio *et al.*, 2010, 2012; Kolotkov, D. Y. *et al.*, 2015) to geophysical systems (Alberti *et al.*, 2014; De Michelis, Consolini, and Tozzi, 2012), in which non-linear and non-stationary processes are present.

Indeed, through the use of the EMD several misleading results can be avoided when local nonstationary and nonlinearity features must be extracted.

References

Adriani, O., Barbarino, G.C., Bazilevskaya, G.A., Bellotti, R., Boezio, M., Bogomolov, E.A., Bonechi, L., Bongi, M., Bonvicini, V., Borisov, S., Bottai, S., Bruno, A., Cafagna, F., Campana, D., Carbone, R., Carlson, P., Casolino, M., Castellini, G., Consiglio, L., De Pascale, M.P., De Santis, C., De Simone, N., Di Felice, V., Formato, V., Galper, A.M., Grishantseva, L., Gillard, W., Jerse, G., Karelin, A.V., Koldashov, S.V., Krutkov, S.Y., Kvashnin, A.N., Leonov, A., Malakhov, V., Marcelli, L., Mayorov, A.G., Menn, W., Mikhailov, V.V., Mocchiutti, E., Monaco, A., Mori, N., Nikonov, N., Osteria, G., Palma, F., Papini, P., Pearce, M., Picozza, P., Pizzolotto, C., Ricci, M., Ricciarini, S.B., Sarkar, R., Rossetto, L., Simon, M., Sparvoli, R., Spillantini, P., Stozhkov, Y.I., Vacchi, A., Vannuccini, E., Vasilyev, G., Voronov, S.A., Wu, J., Yurkin, Y.T., Zampa, G., Zampa, N., Zverev, V.G.: 2011, Observations of the 2006 December 13 and 14 Solar Particle Events in the 80 MeV n^{-1}-3 GeV n^{-1} Range from Space with the PAMELA Detector. *Astrophysical Journal* **742**, 102. DOI. ADS.

Adriani, O., Barbarino, G.C., Bazilevskaya, G.A., Bellotti, R., Boezio, M., Bogomolov, E.A., Bongi, M., Bonvicini, V., Bottai, S., Bruno, A., Cafagna, F., Campana, D., Carbone, R., Carlson, P., Casolino, M., Castellini, G., De Pascale, M.P., De Santis, C., De Simone, N., Di Felice, V., Formato, V., Galper, A.M., Giaccari, U., Karelin, A.V., Kheymits, M.D., Koldashov, S.V., Koldobskiy, S., Krut'kov, S.Y., Kvashnin, A.N., Leonov, A., Malakhov, V., Marcelli, L., Martucci, M., Mayorov, A.G., Menn, W., Mikhailov, V.V., Mocchiutti, E., Monaco, A., Mori, N., Munini, R., Nikonov, N., Osteria, G., Papini, P., Pearce, M., Picozza, P., Pizzolotto, C., Ricci, M., Ricciarini, S.B., Rossetto, L., Sarkar, R., Simon, M., Sparvoli, R., Spillantini, P., Stozhkov, Y.I., Vacchi, A., Vannuccini, E., Vasilyev, G.I., Voronov, S.A., Wu, J., Yurkin, Y.T., Zampa, G., Zampa, N., Zverev, V.G.: 2014, The PAMELA Mission: Heralding a new era in precision cosmic ray physics. *Physics Reports* **544**, 323. DOI. ADS.

Ahn, B.-H., Akasofu, S.-I., Kamide, Y.: 1983, The joule heat production rate and the particle energy injection rate as a function of the geomagnetic indices ae and al. *Journal of Geophysical Research: Space Physics* **88**(A8), 6275. DOI. http://dx.doi.org/10.1029/JA088iA08p06275.

Alberti, T., Lepreti, F., Vecchio, A., Bevacqua, E., Capparelli, V., Carbone, V.: 2014, Natural periodicities and northern hemispheresouthern hemisphere connection of fast temperature changes during the last glacial period: Epica and ngrip revisited. *Climate of the Past* **10**(5), 1751. DOI. http://www.clim-past.net/10/1751/2014/.

Alissandrakis, C.: 1981, On the computation of constant alpha force-free magnetic field. *Astronomy and Astrophysics* **100**, 197.

Araki, T.: *A Physical Model of the Geomagnetic Sudden Commencement.*

Araki T., T.S., T., K.: 2009, Local time variation of the amplitude of geomagnetic sudden commencements (sc) and sc-associated polar cap potential. *Earth, Planets and Space* **61**(4), e13. DOI. http://dx.doi.org/10.1186/BF03353154.

Baransky, L., Borovkov, J., Gokhberg, M., Krylov, S., Troitskaya, V.: 1985, High resolution method of direct measurement of the magnetic field lines' eigen frequencies. *Planetary and space science* **33**(12), 1369.

Bemporad, A., Pagano, P.: 2015, Uncertainties in polarimetric 3D reconstructions of coronal mass ejections. *Astron. Astrophys.* **576**, A93. DOI. ADS.

Berube, D., Moldwin, M.B., Ahn, M.: 2006, Computing magnetospheric mass density from field line resonances in a realistic magnetic field geometry. *Journal of Geophysical Research: Space Physics* **111**(A8), n/a. A08206. DOI. http://dx.doi.org/10.1029/2005JA011450.

Bobra, M.G., Couvidat, S.: 2015, Solar Flare Prediction Using SDO/HMI Vector Magnetic Field Data with a Machine-learning Algorithm. *Astrophys. J.* **798**, 135. DOI. ADS.

Bobra, M.G., Sun, X., Hoeksema, J.T., Turmon, M., Liu, Y., Hayashi, K., Barnes, G., Leka, K.: 2014, The helioseismic and magnetic imager (hmi) vector magnetic field pipeline: Sharps–space-weather hmi active region patches. *Solar Physics* **289**(9), 3549.

Bobra, M.G., Sun, X., Hoeksema, J.T., Turmon, M., Liu, Y., Hayashi, K., Barnes, G., Leka, K.D.: 2014, The Helioseismic and Magnetic Imager (HMI) Vector Magnetic Field Pipeline: SHARPs - Space-Weather HMI Active Region Patches. *Solar Phys.* **289**, 3549. DOI. ADS.

Cane, H.V.: 2000, Coronal mass ejections and forbush decreases. *Space Science Reviews* **93**(1), 55. DOI. http://dx.doi.org/10.1023/A:1026532125747.

Carpenter, D., Anderson, R.: 1992, An isee/ whistler model of equatorial electron density in the magnetosphere. *Journal of Geophysical Research: Space Physics* **97**(A2), 1097.

Carpenter, D.L.: 1963, Whistler evidence of a kneein the magnetospheric ionization density profile. *Journal of Geophysical Research* **68**(6), 1675.

Chi, P., Russell, C., Peterson, W., Le, G., Angelopoulos, V., Reeves, G., Moldwin, M., Chun, F.: 2000, Plasmaspheric depletion and refilling associated with the september 25, 1998 magnetic storm observed by ground magnetometers at l= 2. *Geophysical Research Letters* **27**, 633. DOI. http://dx.doi.org/10.1029/1999GL010722.

Chisham, G., Lester, M., Milan, S.E., Freeman, M.P., Bristow, W.A., Grocott, A., McWilliams, K.A., Ruohoniemi, J.M., Yeoman, T.K., Dyson, P.L., Greenwald, R.A., Kikuchi, T., Pinnock, M., Rash, J.P.S., Sato, N., Sofko, G.J., Villain, J.-P., Walker, A.D.M.: 2007, A decade of the super dual auroral radar network (superdarn): scientific achievements, new techniques and future directions. *Surveys in Geophysics* **28**(1), 33. DOI. http://dx.doi.org/10.1007/s10712-007-9017-8.

Consolini, G., De Michelis, P.: 2005, Local intermittency measure analysis of ae index: The directly driven and unloading component. *Geophysical Research Letters* **32**(5), n/a. L05101. DOI. http://dx.doi.org/10.1029/2004GL022063.

Cristaldi, A., Guglielmino, S.L., Zuccarello, F., Romano, P., Falco, M., van der Voort, L.R., de la Cruz Rodrguez, J., Ermolli, I., Criscuoli, S.: 2014, Dynamic properties along the neutral line of a delta spot inferred from high-resolution observations. *The Astrophysical Journal* **789**(2), 162. http://stacks.iop.org/0004-637X/789/i=2/a=162.

Crooker, N., Cliver, E.: 1994, Postmodern view of m-regions. *Journal of Geophysical Research: Space Physics* **99**(A12), 23383.

Crooker, N., McAllister, A.: 1997, Transients associated with recurrent storms. *Journal of Geophysical Research: Space Physics* **102**(A7), 14041.

Daglis, I., Axford, W., Sarris, E., Livi, S., Wilken, B.: 1997, Particle acceleration in geospace and its association with solar events. *Solar Physics* **172**(1-2), 287.

Davis, T.N., Sugiura, M.: 1966, Auroral electrojet activity index ae and its universal time variations. *Journal of Geophysical Research* **71**(3), 785.

De Michelis, P., Consolini, G., Tozzi, R.: 2012, On the multi-scale nature of large geomagnetic storms: an empirical mode decomposition analysis. *Nonlinear Processes in Geophysics* **19**(6), 667. DOI. http://www.nonlin-processes-geophys.net/19/667/2012/.

De Michelis, P., Tozzi, R., Consolini, G.: 2010, Principal components' features of midlatitude geomagnetic daily variation. *Annales Geophysicae* **28**(12), 2213. DOI. http://www.ann-geophys.net/28/2213/2010/.

Dmitriev, A., Chao, J.-K., Thomsen, M., Suvorova, A.: 2005, Geosynchronous magnetopause crossings on 29–31 october 2003. *Journal of Geophysical Research: Space Physics* **110**(A8).

Dominici P., Z.B. Cander L. R.: 1997, On the origin of medium-period ionospheric waves and their possible modelling: a short review. *Annals of Geophysics* **40**(5), 338. DOI.

Dungey, J.W.: 1961, Interplanetary magnetic field and the auroral zones. *Physical Review Letters* **6**(2), 47.

Ermolli, I., Giorgi, F., Romano, P., Zuccarello, F., Criscuoli, S., Stangalini, M.: 2014, Fractal and multifractal properties of active regions as flare precursors: A case study based on SOHO/MDI and SDO/HMI observations. *Solar Phys.* **289**, 2525. DOI.

Falconer, D.A., Moore, R.L., Gary, G.A.: 2002, Correlation of the Coronal Mass Ejection Productivity of Solar Active Regions with Measures of Their Global Nonpotentiality from Vector Magnetograms: Baseline Results. *Astrophys. J.* **569**, 1016. DOI. ADS.

Feldstein, Y.I., Zaitzev, A.N.: 1968, Quiet and disturbed solar-daily variations of magnetic field at high latitudes during the igy. *Tellus* **20**(2), 338. DOI. http://dx.doi.org/10.1111/j.2153-3490.1968.tb00376.x.

Forbush, S.E.: 1937, On diurnal variation in cosmic-ray intensity. *Terrestrial Magnetism and Atmospheric Electricity* **42**(1), 1. DOI. http://dx.doi.org/10.1029/TE042i001p00001.

Georgoulis, M.K.: 2005, A new technique for a routine azimuth disambiguation of solar vector magnetograms. *The Astrophysical Journal Letters* **629**(1), L69. http://stacks.iop.org/1538-4357/629/i=1/a=L69.

Georgoulis, M.K., LaBonte, B.J.: 2004, Vertical lorentz force and cross-field currents in the photospheric magnetic fields of solar active regions. *The Astrophysical Journal* **615**(2), 1029. http://stacks.iop.org/0004-637X/615/i=2/a=1029.

Giorgi, F., Ermolli, I., Romano, P., Stangalini, M., Zuccarello, F., Criscuoli, S.: 2015, The Signature of Flare Activity in Multifractal Measurements of Active Regions Observed by SDO/HMI. *Solar Phys.* **290**, 507.

Gonzalez, W.D., Tsurutani, B.T., De Gonzalez, A.L.C.: 1999, Interplanetary origin of geomagnetic storms. *Space Science Reviews* **88**(3-4), 529.

Gonzalez, W.D., Joselyn, J.A., Kamide, Y., Kroehl, H.W., Rostoker, G., Tsurutani, B.T., Vasyliunas, V.M.: 1994, What is a geomagnetic storm? *Journal of Geophysical Research: Space Physics* **99**(A4), 5771. DOI. http://dx.doi.org/10.1029/93JA02867.

Gosain, S., Venkatakrishnan, P.: 2010, The evolution of the twist shear and dip shear during x-class flare of 2006 december 13: Hinode observations. *The Astrophysical Journal Letters* **720**(2), L137. http://stacks.iop.org/2041-8205/720/i=2/a=L137.

Gosling, J.T., Bame, S.J., McComas, D.J., Phillips, J.L.: 1990, Coronal mass ejections and large geomagnetic storms. *Geophysical Research Letters* **17**(7), 901. DOI. http://dx.doi.org/10.1029/GL017i007p00901.

Hoeksema, J.T., Liu, Y., Hayashi, K., Sun, X., Schou, J., Couvidat, S., Norton, A., Bobra, M., Centeno, R., Leka, K.D., Barnes, G., Turmon, M.: 2014, The helioseismic and magnetic imager (hmi) vector magnetic field pipeline: Overview and performance. *Solar Physics* **289**(9), 3483. DOI. http://dx.doi.org/10.1007/s11207-014-0516-8.

Huang, N.E., Shen, Z., Long, S.R., Wu, M.C., Shih, H.H., Zheng, Q., Yen, N.-C., Tung, C.C., Liu, H.H.: 1998, The empirical mode decomposition and the hilbert spectrum for nonlinear and non-stationary time series analysis. *Proceedings of the Royal Society of London A: Mathematical, Physical and Engineering Sciences* **454**(1971), 903. DOI. http://rspa.royalsocietypublishing.org/content/454/1971/903.

Hundhausen, A.J.: 1993, Sizes and locations of coronal mass ejections: Smm observations from 1980 and 1984-1989. *Journal of Geophysical Research: Space Physics* **98**(A8), 13177. DOI. http://dx.doi.org/10.1029/93JA00157.

Jiang, C., Wu, S., Feng, X., Hu, Q.: 2016, Data-driven magnetohydrodynamic modelling of a flux-emerging active region leading to solar eruption. *Nature communications* **7**.

Joselyn, J.A., Tsurutani, B.T.: 1990, Geomagnetic sudden impulses and storm sudden commencements: A note on terminology. *Eos, Transactions American Geophysical Union* **71**(47), 1808. DOI. http://dx.doi.org/10.1029/90EO00350.

Kale, Z., Mann, I., Waters, C., Goldstein, J., Menk, F., Ozeke, L.: 2007, Ground magnetometer observation of a cross-phase reversal at a steep plasmapause. *Journal of Geophysical Research: Space Physics* **112**(A10).

Kamide, Y., Kokubun, S.: 1996, Two-component auroral electrojet: Importance for substorm studies. *Journal of Geophysical Research: Space Physics* **101**(A6), 13027.

Kokubun, S.: 1983, Characteristics of storm sudden commencement at geostationary orbit. *Journal of Geophysical Research: Space Physics* **88**(A12), 10025. DOI. http://dx.doi.org/10.1029/JA088iA12p10025.

Kolotkov, D. Y., Nakariakov, V. M., Kupriyanova, E. G., Ratcliffe, H., Shibasaki, K.: 2015, Multi-mode quasi-periodic pulsations in a solar flare. *Astron. Astrophys.* **574**, A53. DOI. http://dx.doi.org/10.1051/0004-6361/201424988.

Kosugi, T., Matsuzaki, K., Sakao, T., Shimizu, T., Sone, Y., Tachikawa, S., Hashimoto, T., Minesugi, K., Ohnishi, A., Yamada, T., *et al.*: 2007, The hinode (solar-b) mission: an overview. *Solar Physics* **243**(1), 3.

Lanzerotti, L., Sayres, D., Medford, L., Maclennan, C., Lepping, R., Szabo, A.: 2000, Response of large-scale geoelectric fields to identified interplanetary disturbances and the equatorial ring current. *Advances in Space Research* **26**(1), 21.

Laurenza, M., Cliver, E., Hewitt, J., Storini, M., Ling, A., Balch, C., Kaiser, M.: 2009, A technique for short-term warning of solar energetic particle events based on flare location, flare size, and evidence of particle escape. *Space Weather* **7**(4).

Lee, D.-Y., Lyons, L.R.: 2004, Geosynchronous magnetic field response to solar wind dynamic pressure pulse. *Journal of Geophysical Research: Space Physics* **109**(A4), n/a. A04201. DOI. http://dx.doi.org/10.1029/2003JA010076.

Leka, K.D., Barnes, G.: 2003, Photospheric Magnetic Field Properties of Flaring versus Flare-quiet Active Regions. I. Data, General Approach, and Sample Results. *Astrophys. J.* **595**, 1277. DOI. ADS.

Leka, K.D., Barnes, G.: 2007, Photospheric Magnetic Field Properties of Flaring versus Flare-quiet Active Regions. IV. A Statistically Significant Sample. *Astrophys. J.* **656**, 1173. DOI. ADS.

Lemen, J.R., Akin, D.J., Boerner, P.F., Chou, C., Drake, J.F., Duncan, D.W., Edwards, C.G., Friedlaender, F.M., Heyman, G.F., Hurlburt, N.E., *et al.*: 2011, The atmospheric imaging assembly (aia) on the solar dynamics observatory (sdo). In: *The Solar Dynamics Observatory*, Springer, ???, 17.

Li, X., Baker, D., Elkington, S., Temerin, M., Reeves, G., Belian, R., Blake, J., Singer, H., Peria, W., Parks, G.: 2003, Energetic particle injections in the inner magnetosphere as a response to an interplanetary shock. *Journal of atmospheric and solar-terrestrial physics* **65**(2), 233.

Lichtenberger, J., Clilverd, M.A., Heilig, B., Vellante, M., Manninen, J., Rodger, C.J., Collier, A.B., Jrgensen, A.M., Reda, J., Holzworth, R.H., Friedel, R., Simon-Wedlund, M.: 2013, The plasmasphere during a space weather event: first results from the plasmon project. *J. Space Weather Space Clim.* **3**, A23. DOI. http://dx.doi.org/10.1051/swsc/2013045.

Lites, B., Casini, R., Garcia, J., Socas-Navarro, H.: 2007, A suite of community tools for spectro-polarimetric analysis. *Memorie della Societa Astronomica Italiana* **78**, 148.

Lites, B., Akin, D., Card, G., Cruz, T., Duncan, D., Edwards, C., Elmore, D., Hoffmann, C., Katsukawa, Y., Katz, N., *et al.*: 2013, The hinode spectro-polarimeter. *Solar Physics* **283**(2), 579.

Lorentzen, K., Mazur, J., Looper, M., Fennell, J., Blake, J.: 2002, Multisatellite observations of mev ion injections during storms. *Journal of Geophysical Research: Space Physics* **107**(A9).

Menk, F., Kale, Z., Sciffer, M., Robinson, P., Waters, C., Grew, R., Clilverd, M., Mann, I.: 2014, Remote sensing the plasmasphere, plasmapause, plumes and other features using ground-based magnetometers. *Journal of Space Weather and Space Climate* **4**, A34.

Moldwin, M.B.: 1997, Outer plasmaspheric plasma properties: What we know from satellite data. *Space Science Reviews* **80**(1), 181. DOI. http://dx.doi.org/10.1023/A:1004921903897.

Moran, T.G., Davila, J.M.: 2004, Three-Dimensional Polarimetric Imaging of Coronal Mass Ejections. *Science* **305**, 66. DOI. ADS.

O'Brien, T., Moldwin, M.: 2003, Empirical plasmapause models from magnetic indices. *Geophysical research letters* **30**(4).

Park, C.: 1973, Whistler observations of the depletion of the plasmasphere during a magnetospheric substorm. *Journal of geophysical research* **78**(4), 672.

Park, C.G.: 1974, Some features of plasma distribution in the plasmasphere deduced from antarctic whistlers. *Journal of Geophysical Research* **79**(1), 169. DOI. http://dx.doi.org/10.1029/JA079i001p00169.

Patel, V.L., Coleman, P.J.: 1970, Sudden impulses in the magnetosphere observed at synchronous orbit. *Journal of Geophysical Research* **75**(34), 7255. DOI. http://dx.doi.org/10.1029/JA075i034p07255.

Pesnell, W.D., Thompson, B.J., Chamberlin, P.C.: 2012, The solar dynamics observatory (sdo). *Solar Physics* **275**(1), 3. DOI. http://dx.doi.org/10.1007/s11207-011-9841-3.

Petrie, G.: 2012, The abrupt changes in the photospheric magnetic and lorentz force vectors during six major neutral-line flares. *The Astrophysical Journal* **759**(1), 50.

Piersanti, M., Villante, U.: 2016, On the discrimination between magnetospheric and ionospheric contributions on the ground manifestation of sudden impulses. *Journal of Geophys-*

ical Research: Space Physics **121**(7), 6674. 2015JA021666. DOI. http://dx.doi.org/10.1002/2015JA021666.

Reames, D.V.: 2013, The Two Sources of Solar Energetic Particles. *Space Science Reviews* **175**, 53. DOI. ADS.

Romano, P., Zuccarello, F.P., Guglielmino, S.L., Zuccarello, F.: 2014, Evolution of the magnetic helicity flux during the formation and eruption of flux ropes. *The Astrophysical Journal* **794**(2), 118. http://stacks.iop.org/0004-637X/794/i=2/a=118.

Ruohoniemi, J.M., Baker, K.B.: 1998, Large-scale imaging of high-latitude convection with super dual auroral radar network hf radar observations. *Journal of Geophysical Research: Space Physics* **103**(A9), 20797. DOI. http://dx.doi.org/10.1029/98JA01288.

Ruohoniemi, J.M., Greenwald, R.A.: 1996, The response of high-latitude convection to a sudden southward imf turning. *Geophysical Research Letters* **25**(15), 2913. DOI. http://dx.doi.org/10.1029/98GL02212.

Scherrer, P.H., Schou, J., Bush, R.I., Kosovichev, A.G., Bogart, R.S., Hoeksema, J.T., Liu, Y., Duvall, T.L., Zhao, J., Title, A.M., Schrijver, C.J., Tarbell, T.D., Tomczyk, S.: 2012, The helioseismic and magnetic imager (hmi) investigation for the solar dynamics observatory (sdo). *Solar Physics* **275**(1), 207. DOI. http://dx.doi.org/10.1007/s11207-011-9834-2.

Schrijver, C.J.: 2007, A Characteristic Magnetic Field Pattern Associated with All Major Solar Flares and Its Use in Flare Forecasting. *Astrophys. J. Lett.* **655**, L117. DOI. ADS.

Schrijver, C.J.: 2009, Driving major solar flares and eruptions: A review. *Advances in Space Research* **43**, 739. DOI. ADS.

Schrijver, C.J., DeRosa, M.L.: 2003, Photospheric and heliospheric magnetic fields. *Solar Physics* **212**(1), 165. DOI. http://dx.doi.org/10.1023/A:1022908504100.

Sheeley, N.R., Howard, R.A., Koomen, M.J., Michels, D.J., Schwenn, R., Mhlhuser, K.H., Rosenbauer, H.: 1985, Coronal mass ejections and interplanetary shocks. *Journal of Geophysical Research: Space Physics* **90**(A1), 163. DOI. http://dx.doi.org/10.1029/JA090iA01p00163.

Shepherd, S., Greenwald, R., Ruohoniemi, J.: 2002, Cross polar cap potentials measured with super dual auroral radar network during quasi-steady solar wind and interplanetary magnetic field conditions. *Journal of Geophysical Research: Space Physics* **107**(A7). DOI. http://dx.doi.org/10.1029/2001JA000109.

Shue, J.-H., Song, P., Russell, C., Steinberg, J., Chao, J., Zastenker, G., Vaisberg, O., Kokubun, S., Singer, H., Detman, T., *et al.*: 1998, Magnetopause location under extreme solar wind conditions. *Journal of Geophysical Research: Space Physics* **103**(A8), 17691.

Suvorova, A., Dmitriev, A., Chao, J.-K., Thomsen, M., Yang, Y.-H.: 2005, Necessary conditions for geosynchronous magnetopause crossings. *Journal of Geophysical Research: Space Physics* **110**(A1).

Terradas, J., Oliver, R., Ballester, J.L.: 2004, Application of statistical techniques to the analysis of solar coronal oscillations. *The Astrophysical Journal* **614**(1), 435. http://stacks.iop.org/0004-637X/614/i=1/a=435.

Tsuneta, S., Ichimoto, K., Katsukawa, Y., Nagata, S., Otsubo, M., Shimizu, T., Suematsu, Y., Nakagiri, M., Noguchi, M., Tarbell, T., Title, A., Shine, R., Rosenberg, W., Hoffmann, C., Jurcevich, B., Kushner, G., Levay, M., Lites, B., Elmore, D., Matsushita, T., Kawaguchi, N., Saito, H., Mikami, I., Hill, L.D., Owens, J.K.: 2008, The solar optical telescope for the hinode mission: An overview. *Solar Physics* **249**(2), 167. DOI. http://dx.doi.org/10.1007/s11207-008-9174-z.

Tsyganenko, N.: 2002, A model of the near magnetosphere with a dawn-dusk asymmetry 1. mathematical structure. *Journal of Geophysical Research: Space Physics* **107**(A8).

Tsyganenko, N.A., Sitnov, M.I.: 2005, Modeling the dynamics of the inner magnetosphere during strong geomagnetic storms. *Journal of Geophysical Research: Space Physics* **110**(A3), n/a. A03208. DOI. http://dx.doi.org/10.1029/2004JA010798.

Valtonen, E.: 2005, Space weather effects on technology. In: *Space Weather*, Springer, ???, 241.

Vecchio, A., Laurenza, M., Carbone, V., Storini, M.: 2010, Quasi-biennial modulation of solar neutrino flux and solar and galactic cosmic rays by solar cyclic activity. *The Astrophysical Journal Letters* **709**(1), L1. http://stacks.iop.org/2041-8205/709/i=1/a=L1.

Vecchio, A., Laurenza, M., Meduri, D., Carbone, V., Storini, M.: 2012, The dynamics of the solar magnetic field: Polarity reversals, butterfly diagram, and quasi-biennial oscillations. *The Astrophysical Journal* **749**(1), 27. http://stacks.iop.org/0004-637X/749/i=1/a=27.

Vellante, M., Förster, M.: 2006, Inference of the magnetospheric plasma mass density from field line resonances: A test using a plasmasphere model. *Journal of Geophysical Research: Space Physics* **111**(A11).

Vellante, M., Piersanti, M., Pietropaolo, E.: 2014, Comparison of equatorial plasma mass densities deduced from field line resonances observed at ground for dipole and igrf models. *Journal of Geophysical Research: Space Physics* **119**(4), 2623. 2013JA019568. DOI. http://dx.doi.org/10.1002/2013JA019568.

Villante, U., Piersanti, M.: 2008, An analysis of sudden impulses at geosynchronous orbit. *Journal of Geophysical Research: Space Physics* **113**(A8), n/a. A08213. DOI. http://dx.doi.org/10.1029/2008JA013028.

Villante, U., Piersanti, M.: 2009, Analysis of geomagnetic sudden impulses at low latitudes. *Journal of Geophysical Research: Space Physics* **114**(A6), n/a. A06209. DOI. http://dx.doi.org/10.1029/2008JA013920.

Wang, H., Ewell Jr, M., Zirin, H., Ai, G.: 1994, Vector magnetic field changes associated with x-class flares. *The Astrophysical Journal* **424**, 436.

Wanliss, J.A., Showalter, K.M.: 2006, High-resolution global storm index: Dst versus sym-h. *Journal of Geophysical Research: Space Physics* **111**(A2), n/a. A02202. DOI. http://dx.doi.org/10.1029/2005JA011034.

Waters, C.L., Menk, F.W., Fraser, B.J.: 1991, The resonance structure of low latitude pc3 geomagnetic pulsations. *Geophysical Research Letters* **18**(12), 2293. DOI. http://dx.doi.org/10.1029/91GL02550.

Webb, D., Cliver, E., Crooker, N., St Cyr, O., Thompson, B.: 2000, Relationship of halo coronal mass ejections, magnetic clouds, and magnetic storms. *Journal of Geophysical Research: Space Physics* **105**(A4), 7491.

Zhang, J., Wang, J.: 2002, Are homologous flare-coronal mass ejection events triggered by moving magnetic features? *The Astrophysical Journal Letters* **566**(2), L117.

Zuccarello, F., Romano, P., Farnik, F., Karlicky, M., Contarino, L., Battiato, V., Guglielmino, S., Comparato, M., Ugarte-Urra, I.: 2009, The x17. 2 flare occurred in noaa 10486: an example of filament destabilization caused by a domino effect. *Astronomy & Astrophysics* **493**(2), 629.